

Chapter 6

The Inverse Problem: Using Spectral Theory to Recover the Atmospheric Refractivity Profile

6.1 Introduction

Throughout Chapter 5, we mostly were concerned with the use of a full spectral representation of the electromagnetic field. We are not unmindful, however, of the potential suitability of this particular spectral technique to the inverse problem: determining the bending-angle and refractivity profiles from a time sequence of measurements of amplitude and phase of the received signal. This is especially interesting when adverse signal conditions prevail, that is, when the received signal exhibits significant amplitude and phase interference from multiple rays. In these situations, classical recovery algorithms, such as those using the excess Doppler with the Abel transform, can run into difficulty because of the non-uniqueness or even non-existence of the ray path. Caustic points also lead to a breakdown in the validity of geometric optics, i.e., second-order ray theory, on which the Abel transform algorithm is based. Spectral techniques, whether they are rooted in geometric optics or in a full-spectrum wave theory, can deal with these types of propagation problems. Although multiple rays with different bending angles can arrive at the low Earth orbiting (LEO) spacecraft at the same time, they cannot arrive simultaneously with the same excess Doppler values when spherical symmetry applies; those must be distinct. The transformation of the time series of observations into a spectral series provides a means to uniquely recover bending-angle and refractivity profiles because of this one-to-one relationship between bending angle and excess Doppler.

In this chapter, we briefly outline the use of the particular full-spectrum wave theory technique developed in Chapter 5 for the inverse problem. The spectral density function $G[\rho, \nu]$, which is the extra phase delay at the radial position r induced by the refractivity gradient on the ν th spectral component of the wave, plays a central role. We will not discuss in detail the computational aspects using this particular spectral technique, nor the concomitant use of estimation theory techniques on noisy data.

We assume that the LEO has received an ordered time series of amplitude and phase measurements, appropriately stripped of the geometric LEO/Global Positioning System (GPS) Doppler signature and any other contributory error sources. For example, we assume perfect orbit knowledge from precision orbit determination (POD). We assume that the effects of oscillator variations in the various clocks affecting the phase measurements have been eliminated through redundant differential tracking, and we assume that ionospheric effects can be eliminated through dual-band L1 and L2 tracking, possibly supplemented with modeling to eliminate third-order effects. We also assume that the signal-to-noise ratio (SNR) of the signal is sufficient for a Nyquist sample rate to be practicable with respect to the bandwidth of the particular atmospheric signature under study.

Although this chapter does discuss a stand-alone Fourier approach for the inverse problem with radio occultation data, we note again that a principal utility of radio occultation data is for meteorology and numerical weather prediction. There the occultation data are merged in a timely way into a much richer and broader multi-sensor database, which is constrained by a comprehensive model that characterizes the atmosphere and controls atmospheric processes. This already is mentioned in Chapter 1. In this context, the difference between an actual radio occultation observation (phase, amplitude, etc.) and a predicted observation obtained by forward propagation of the GPS signal through the atmospheric model becomes a constraint among the free parameters of the model. The four-dimensional variational analysis (4DVAR) methodology for minimizing a quadratic cost function involving disparate competing databases constrained by the model is central to accurate weather prediction [1]. In this application, one usually would not recover the refractivity profile from a radio occultation profile alone, but only from within the 4DVAR context. Nevertheless, the stand-alone approach has some important uses, and it is discussed in the next sections.

6.2 GPS Receiver Operations

It is helpful to understand some basic operational aspects of the GPS receiver in measuring phase and amplitude. The BlackJack GPS receiver series is a modern, high accuracy, dual-band, digital receiver developed by the Jet Propulsion Laboratory (JPL) for scientific applications in space. As its

development has evolved over the past several years, it has successfully flown on over one-half dozen Earth satellites for navigation and timekeeping, precision orbit determination, geopotential mapping, ocean reflections, and limb sounding [2].

The following is a rather high-level account of this particular receiver. It omits important details, which are crucial to the actual recovery of atmospheric parameters, but which are less relevant to the discussion here, e.g., dual-frequency tracking to remove ionosphere effects, dealing with clock errors, digital signal processing, and correlation operations on noisy data [3,4].

In normal operations, the BlackJack receiver uses a closed-loop phase model before extracting the phase delay information to reduce the frequency of the received radio frequency (RF) signal from the GPS satellite to base band, a few tens of hertz. First, the received RF signal (carriers in the 1.2 to 1.6 GHz range) is 1-bit digital sampled in-phase and separately in-quadrature, that is, with the received RF phase shifted by 90 deg. To facilitate the signal processing by the receiver, the carrier frequency in these two parallel bit streams is reduced to an intermediate frequency (IF) of around 200 kHz, which is then further reduced to the base band frequency using an in-receiver phase model. This model is generated from a cubic polynomial fit to previous phase measurements made by the receiver over the past few tens of milliseconds, and in the closed-loop mode it is updated after each observational epoch with the latest phase measurement [4].

The L1 (1575 MHz) and L2 (1226 MHz) carriers of the navigation signals from each GPS satellite are derived from the same onboard master oscillator, and, therefore, they are initially coherent. The L1 carrier is phase modulated coherently with the clear access (C/A) and precision (P) ranging codes. The L2 carrier is phase-modulated with only the P code (on the present generation of GPS satellites), but coherently with the L1. These ranging codes are pseudorandom, phase-modulating square waves that fully suppress the carrier tone. Each transition of a code, occurring at a frequency or chip rate of 1.023 MHz for the C/A code and at 10.23 MHz for the P code, involves a change in phase of the carrier of either 0 deg or 180 deg in accordance with the pseudorandom algorithm specific to that particular code. Both carriers also are phase modulated with a header code operated at a 50-Hz chip rate. This very low rate code carries the almanac and timing information for the tracked satellite and other satellite health and housekeeping data. Each satellite broadcasts distinctive codes that are unique to that satellite. These codes are mutually orthogonal, and they also are orthogonal between GPS satellites. In the limit, cross-correlating two different codes yields a null result. Moreover, because the codes are pseudorandom, their auto-correlation function is triangular across an alignment offset of up to ± 1 chip period, and its value is zero outside of this range. This means that multiplying the same code with itself but time shifted also yields a null result unless the two components are aligned

within ± 1 chip period, the spatial equivalent of about ± 30 m for the P code. Therefore, cross-correlating the received signal from a specific GPS satellite with the appropriately time- and Doppler-shifted C/A and P code replicas effectively filters out the signals received from all other satellites and also signals with phase delay offsets greater than the chip period. Also, by aligning the codes, it enables a determination of the propagation delay between that satellite and the receiver plus any timekeeping difference between their clocks.

The base band signal embedded in the in-phase and the quadrature bit streams being processed by the receiver is a composite of all broadcasting GPS satellites in view of the receiver's antennas. Also, the sign of each bit, +1 or -1, is dominated by the inevitable thermal or SNR noise on the original RF sampling process. Each of these bi-level bit streams is multiplied on a bit-by-bit basis by the time-delayed and Doppler-shifted base band replica of the actual signal broadcast from a specific GPS satellite. These products then are averaged over a given time interval, i.e., they are cross-correlated. The nominal averaging time for this cross-correlation is 20 ms. The receiver can perform this operation in parallel on the dual-band L1 and L2 signals from up to a dozen individual GPS satellites. The cross-correlation operation accomplishes three objectives. First, the signals from all other satellites are essentially filtered out. Second, when the time-delayed and Doppler-shifted base band replica is aligned with the arriving signal from that specific satellite, the effective SNR noise on the correlation products for that satellite is averaged down. Third, the alignment returning the maximum value of the correlation product provides the difference of the reception epoch of the receiver clock minus the transmission epoch of the clock onboard the GPS satellite. Synchronizing the transmitter and receiver clocks then allows the propagation delay, or group delay, from that satellite to the receiver to be obtained. Clock synchronization is achieved through redundant concurrent tracking of selected GPS satellites, including the occulted satellite, from the LEO receiver and from the global network of ground station receivers. Concurrent tracking of multiple GPS satellites from multiple receivers allows determination of the clock epoch differences. This cross-correlation between the received signal and its replica from a given satellite is performed on the in-phase bit stream and also separately on the quadrature bit stream. Thus, during 20 ms on each bit stream, the signal is averaged over 20,000 transition points or chip periods of the C/A code and 200,000 chip periods of the P code. The noise error in the average is inversely proportional to the square root of the averaging interval.

The propagation delay between the broadcasting GPS satellite and the receiver may be determined in two ways. The alignment of the bit streams, so that the autocorrelation function described above from the received and replica codes is maximized, yields the group delay plus SNR error. After the autocorrelation function is maximized, a far more precise determination of propagation delay is obtained from the measurement of the phase of the carrier

itself, which has a wavelength of only about 20 cm; in comparison, the “wavelength” of the P code is about 30 m. This propagation delay of the carrier phase is obtained from the two time-averaged correlation coefficients, the in-phase coefficient (I) and the quadrature coefficient (Q). The arctangent of I divided by Q gives a measurement of the difference in true phase minus the phase predicted from the in-receiver model, modulo 2π .¹ If no cycles are lost between the epochs of the current measurement and the immediate previous measurement 20 ms earlier, adding the predicted phase from the model to the measured phase difference gives the true phase plus the averaged-down SNR error at that observation epoch. An important property of this scheme (adding the predicted phase to the measured difference) is that the SNR measurement error of the true phase at each observation epoch is statistically independent of the SNR error at any other epoch. The root-sum-square of the in-phase and quadrature correlation coefficients gives the amplitude of the signal. The SNR error on the phase measurement is statistically uncorrelated with the SNR error on the amplitude measurement. These measurements of true phase and amplitude then are reported by the receiver at a nominal sample rate of every 20 ms; this is a convenient reporting rate because of the 50-Hz header code. Other multiples of that canonical sample interval can be used.

This closed-loop correlation and reporting scheme for the phase works well when the root-mean-square (rms) difference between the predicted and measured phase is small, substantially less than 1/4 cycle. In this case, there is a very high probability that no complete cycles, of either a positive or negative integer number, have been unaccounted for between the two successive measurement epochs. Using Gaussian statistics, it is easy to show why this is so. Suppose that the measured phase at a particular epoch differed from the predicted value by exactly 1/2 cycle. Then we would have no way of determining whether that measurement was a cycle above or a cycle below the predicted value; all cycles look alike. Regarding this measured 1/2 cycle difference, do we add it to or subtract it from the predicted phase given by the model? Suppose that the statistical difference between measured and predicted

¹ In early versions of the BlackJack receiver, a simpler 2-quadrant arctangent routine without complete 4-quadrant resolution was used on the I and Q correlation coefficients to extract phase. This design choice eliminated the requirement to determine during the signal processing the sign of the 50-Hz header code bit ± 1 . An error in its sign affects the sign of the I and Q correlation products the same way, and cancels in their ratio. But, this results in a 1/2-cycle ambiguity. This exacerbates the cycle slipping problem in noisy and/or loop-stressed conditions. Unfortunately, this 2-quadrant arctangent operation has resided in the digital signal processing firmware—the application-specific integrated circuits (ASICs)—of the receiver, which is not easily modified without incurring the expense of redesigning and fabricating the ASIC at a silicon foundry. BlackJack designers at JPL plan to incorporate a 4-quadrant discriminator in a future version. The discussion here assumes the 4-quadrant version.

phase, arising from either SNR errors or from unknown phase acceleration or from both, turns out to be $1/4$ cycle, $1 - \sigma$. Then the probability of getting less than $1/2$ cycle difference at each measurement epoch, if the errors are Gaussian distributed, is $\text{erf}[2 / 2^{1/2}]$, or 0.9545. It follows that the probability of having at least one difference that is greater than $1/2$ cycle after n successive statistically independent samples is $1 - 0.9545^n$. After 1 s of elapsed time at a rate of 1 sample per 20 ms, $n = 50$; therefore, for $\sigma = 1/4$ cycle, the probability of getting at least one phase difference greater than $1/2$ cycle in 50 trials is virtually certain. If at a given measurement epoch the measured phase difference is $1/2$ cycle, then there is at least a 50 percent chance of choosing the wrong integer for the cumulative cycle count. Therefore, for $\sigma = 1/4$ cycle, a non-zero integer number of cycle slips becomes virtually certain within 1 s with a 20 ms sample interval. On the other hand, suppose the $1 - \sigma$ value of the statistical difference between the measured and predicted phase is $1/8$ cycle. Then the probability of getting one or more phase differences that are greater than $1/2$ cycle in n successive samples is $1 - \text{erf}[4 / 2^{1/2}]^n = 1 - 0.9968^n$, still nearly zero for $n = 50$. In good signal conditions with small differences between measured and predicted phase, this scheme (of adding the predicted phase to the measured difference modulo 2π) usually works well.

6.2.1 Adverse Signal Conditions

A problem arises in adverse signal conditions, for example, when more than one ray arrives concurrently at the LEO, leading to interference and to sharp accelerations in phase across the troughs in the amplitude scintillation. Another adverse condition is where the LEO enters a quasi-shadow zone where no rays or at most highly defocused rays are present. Interference scenarios have been described earlier in Figs. 5-19 through 5-34. Figure 5-34 shows a specific example of fringe frequencies of roughly 50 Hz, 1 cycle change over 20 ms. Reducing the refractivity gradient in this model by a factor of four to obtain more realistic conditions, that is, ones that are more closely aligned with the Earth's atmosphere, quadruples the length of time. Thus, $1/4$ cycle change occurs for this relaxed case in 20 ms, which still is a potential problem for closed-loop operations. This level of phase acceleration is serious enough to cause, with some probability on each correlation interval, at least one cycle not to be properly added or subtracted from the integer count book kept by the in-receiver phase model. Over the many successive 20-ms sample intervals spanning a few seconds, this could amount to a significant number of systematically lost cycles.

Consider the Gaussian refractivity model used in Fig. 5-20 and also the composite Gaussian/exponential model in Fig. 5-26. For a Gaussian distribution, the impact parameter separations between rays in the multipath

zone scale roughly linearly with the $1 - \sigma$ width H_w of the distribution, but the width of the multipath zone (in θ_L or in elapsed time) scales roughly as $H_w^{-3/2}$. The separations between rays scale only weakly with N_w , but the width of the zone scales nearly linearly with N_w . For the impact parameter diagram shown in Fig. 5-20, the values used are $N_w = 0.0001$ and $H_w = 1.6$ km, which results in impact parameter separations of roughly 10 km, rather large compared to realistic scenarios. But, in Fig. 5-26, the values used in the Gaussian component are $N_w = 0.00005$ and $H_w = 350$ m, corresponding to a peak water vapor number density of about 1 percent of the local dry air density. More importantly, for Fig. 5-26, this component is superimposed on a background refracting medium that is defocusing, an exponential profile corresponding to dry air. This composite model leads to impact parameter separations in the multipath zone of up to 3 km or to excess Doppler differences of up to about 15 Hz, or 1/3 cycle in 20 ms.

Another adverse signal situation occurs when the LEO encounters a shadow zone with weak signal conditions followed by flaring and strong interference. Consider a local refracting medium (e.g., a water vapor layer) embedded in an ambient medium (e.g., dry air) that gives rise to the transient in Fig. 6-1, which shows bending angle versus impact parameter. An abrupt increase in refractivity below a spherical boundary could yield this form for the bending-angle profile. Here $\rho_o = k(1 + N_o)r_o$ corresponds to sea level. N_o is the refractivity for dry air at sea level. The exponential model in Eq. (5.8-2a) is used here for the dry air component of the refractivity with $N_o = 0.00027$ and the scale height $Hk^{-1} = 7$ km. Below the boundary at $r_o + Hk^{-1}/4$, about 2 km above sea level, the total refractivity abruptly increases, but then with decreasing altitude its gradient gradually approaches the dry air gradient. (Figure 6-7 later in this chapter shows the recovered refractivity profile for this water vapor layer.)

The impact parameter diagram shown in Fig. 6-2 results from the same bending-angle profile shown in Fig. 6-1. The values of the refractivity and orbit parameters are the same for Figs. 6-1 through 6-7. The LEO orbit radius is $r_L = 1.1r_o$. Here θ_{ρ_o} marks the angular position of the LEO when located on the refracted shadow boundary, and it is defined by Bouguer's law, $\rho_o = \rho_L \sin(\theta_{\rho_o} + \alpha_L(\rho_o))$. Here $\rho_L = kr_L$, and $\alpha_L(\rho_o)$ is the refractive bending angle observed by the LEO at $\theta_L = \theta_{\rho_o}$. This figure, expressed in terms of impact parameter altitude in kilometers versus orbit angle, provides an example of a shadow zone (where $d\rho_*/d\theta_L \approx 0$) followed by caustic flaring and multipath. At $r \approx r_o + H/4k$, the main ray (m) encounters a sharp increase in refractivity as its tangency point descends below a boundary there. The abrupt increase in refractive bending at this boundary causes a shadow zone. As θ_L

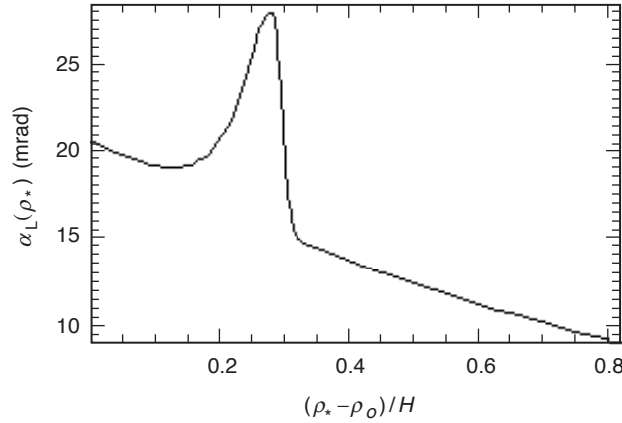


Fig. 6-1. Hypothetical bending angle at the LEO for a layer of higher refractivity embedded in dry air near sea level. Figure 6-7 shows the recovered refractivity profile for this water vapor layer.

further decreases, the first caustic is encountered at $\theta_L - \theta_{\rho_o} \approx 2$ mrad, leading to the creation of two more rays (a) and (b) in addition to the main ray (m). For a coplanar geometry, the Doppler difference between these new rays and the (m) ray is 6 to 7 Hz at the first contact point; it gradually increases as the rays separate. This difference is given by $\Delta f_{b-m} = (\rho_{*m} - \rho_{*b}) \dot{\theta}_L / 2\pi$, where $\dot{\theta}_L$ is the LEO angular velocity in the plane of incidence. Interference continues until the (a) and (m) rays disappear below the lower caustic point at $\theta_L - \theta_{\rho_o} \approx -7$. This scenario has been discussed in more detail in Chapter 2 using a thin phase screen and scalar diffraction theory—in particular, in Figs. 2-2(c) and 2-11. In the case shown here in Fig. 6-2, the (a) and (b) rays created at the right-hand caustic point have phases at the LEO that differ by many cycles from the phase of the main ray (m). Moreover, they also have substantially lower excess Doppler frequencies. In this figure, the difference is 6 to 7 Hz initially for a coplanar geometry, and it grows to 15 Hz as the altitude of the (b) ray impact parameter separates from the other two. When the occulted GPS satellite does not lie in the LEO orbit plane, obliquity effects reduce this Doppler level by up to about 30 percent; see Eq. (6.3-4) and Fig. 6-8.

Figure 6-3 shows the amplitude of the field at the LEO that results from this transient in the bending angle shown in Fig. 6-1. The amplitude of the main field, which has a vacuum value of unity, has been defocused down to about 0.4 by the dry air refractivity profile. In this example, the upper caustic (right) yields strong signal flaring, but flaring from the lower caustic (left) is more muted because of the larger curvature in the impact parameter curve there (see Fig. 6-2). The voltage SNR well into the shadow zone is about 11 dB below the

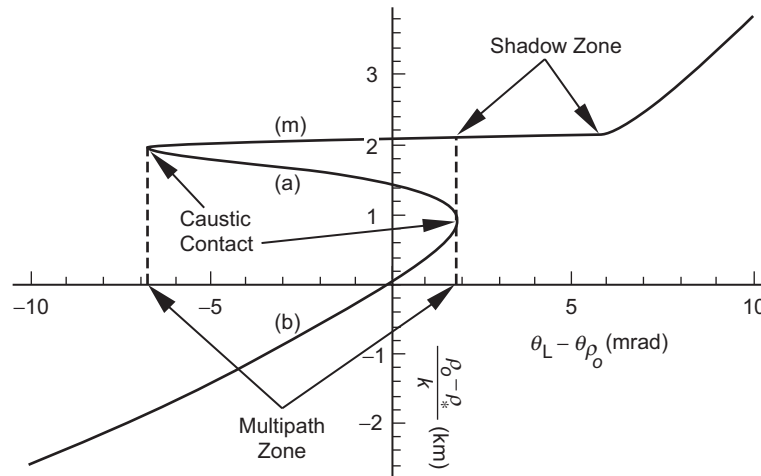


Fig. 6-2. Impact parameter diagram for the refractive bending-angle profile given in Fig. 6-1.

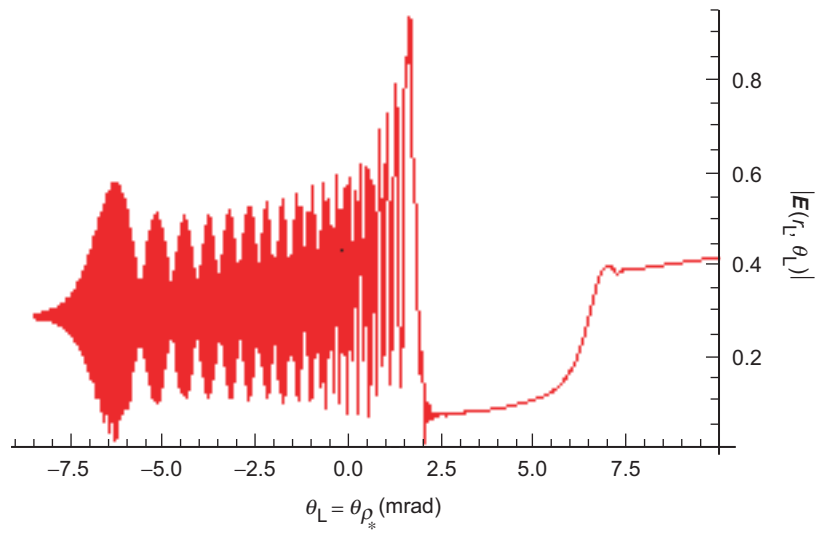


Fig. 6-3. Amplitude of the field at the LEO from the bending-angle profile given in Fig. 6-1.

voltage SNR for GPS signals in a vacuum. Diffraction creates edge fringes, but it also softens rough edges, resulting in the more gradual decay of SNR at the beginning of the shadow boundary.

Figure 6-4 shows the phase difference between the complete field and the field from the main ray (m) only. This figure begins near the end of the shadow zone and includes the contact with the first caustic. For a coplanar geometry, this figure covers about 3 to 4 s of elapsed time. The excess Doppler for the (m) ray becomes nearly constant at entry into the shadow zone. In fact, a ray with nearly constant excess Doppler is a very defocused ray [see Eq. (6.3-11)]. In the lower troposphere, defocusing from the dry air refractivity gradient compresses the wider altitude differences of these impact parameters. Nevertheless, this figure shows an abrupt change in Doppler, within a 20- to 30-msec interval, from 0 Hz to about 7 Hz for a coplanar geometry.

Figure 6-5 shows a blowup of the amplitude and phase of the field at the LEO in Figs. 6-3 and 6-4 in the vicinity of $\theta_L - \theta_{\rho_o} = 2.1$ around a very deep amplitude trough in the interference fringes. Here the emerging (a) and (b) rays, still essentially coherent and at a point slightly earlier than the geometric optics prediction of the caustic contact point, have strengthened so that their combined amplitude at the point where their phase is opposite the phase of the (m) ray nearly matches its amplitude. This causes a near-complete cancellation of the total field and a short burst of rapid phase acceleration. The black dots in the figure denote measurement epochs on 20-ms centers (for $d\tilde{\theta}_L/dt = -1$ mrad/s). The gray-scale dots are predicted phase values at future epochs. The SNR error bars are relative; their actual values also depend on signal strength and processing technique. In these situations,

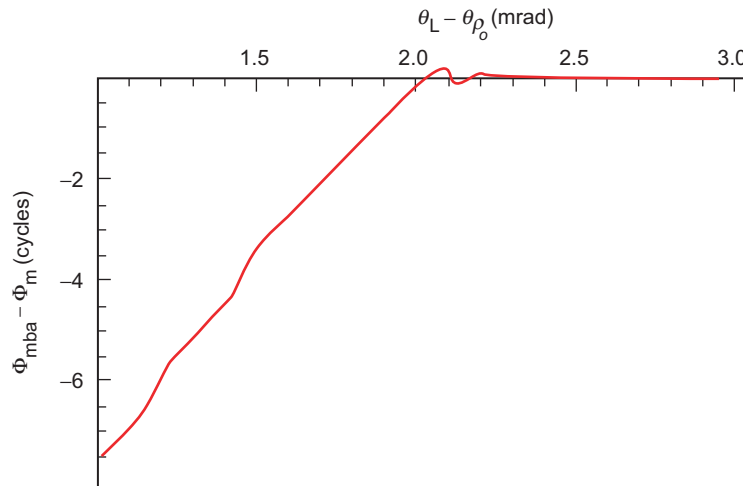


Fig. 6-4. Phase of the complete field at the LEO minus the phase of the main ray (m) resulting from the Fig. 6-1 bending-angle profile.

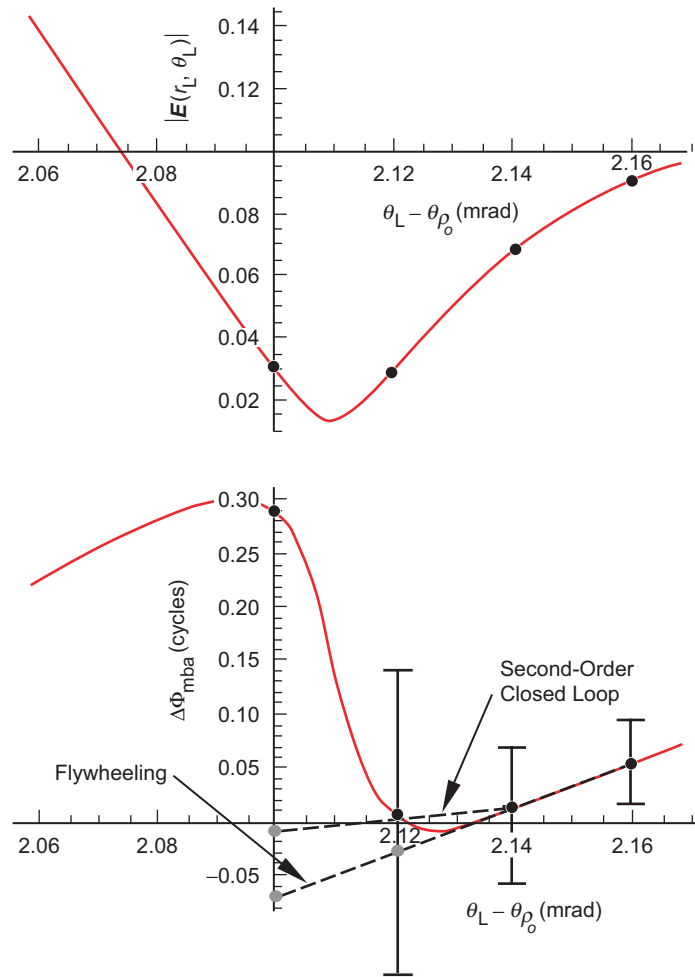


Fig. 6-5. Blowup of Figs. 6-3 and 6-4 at $\theta_L - \theta_{p_0} \approx 2.1$ showing the burst of phase acceleration at $\theta_L - \theta_{p_0} = 2.12$ resulting from near-complete cancellation of the field caused by interference between the main ray and the opposing caustic rays.

the rms disparity between predicted and measured phase can exceed 1/4 cycle primarily because of the inability of the in-receiver phase model to anticipate adequately the phase acceleration from interference between these multiple rays, and because of poor SNR noise in the phase measurement. Reducing the sample time to mitigate phase acceleration effects and to catch stray cycles adversely impacts the effective SNR of the sampled measurement, which further exacerbates the potential disparity.

Multipath situations like these have led the BlackJack designers to experiment with alternate sampling and reporting schemes, such as flywheeling the receiver. An additional technique is to use a realistic excess Doppler algorithm combined with the receiver fractional phase measurement to connect phase. Other open-loop schemes are feasible; the receiver uses a realistic in-receiver model and simply reports multiple time-lagged correlation coefficients in an open-loop mode. This approach leaves it to the data analysts to recover the various phases from the multiple rays relative to the realistic model and also to extract their respective amplitudes.

6.2.2 Flywheeling

Flywheeling uses an extrapolation from the in-receiver phase model, set at an earlier time where the phase was considered to be unambiguous, to predict the phase at a future epoch, without updating the model with new information from the most recent epoch because of its uncertainty. Both the closed-loop and the flywheeling modes are depicted in Fig. 6-5. To simplify the figure, only a second-order loop is shown, which is indicated by the sloped straight lines. But the receiver actually uses a third-order technique to predict forward; the extrapolation lines in this figure should be curved. In this simpler form of the in-receiver model, the phase measurements from the previous two measurement epochs are used to set the Doppler and the phase. In Fig. 6-5, these two points are located at $\theta_L - \theta_{\rho_o} = 2.14$ and 2.16 mrad. In this figure, time evolves to the left for a setting occultation at a rate of roughly -1 s/mrad for a coplanar occultation. Thus, the abscissa can be read directly in seconds of time. For a non-coplanar case, the time scale would be compressed by the obliquity; for a 30-deg LEO orbit-plane inclination relative to the plane of incidence, the elapsed time interval in this figure would be 30 percent greater (see Fig. 6-8). In the closed-loop mode, the receiver uses the measured phase at these two earlier epochs at $\theta_L - \theta_{\rho_o} = 2.14$ and 2.16 to predict the phase at the next epoch at $\theta_L - \theta_{\rho_o} = 2.12$. Upon obtaining the new phase measurement at this later epoch, it then updates the Doppler and phase of the model to predict the phase at $\theta_L - \theta_{\rho_o} = 2.10$. In the flywheeling mode, the receiver does not update the model at $\theta_L - \theta_{\rho_o} = 2.12$, and it extrapolates the model fixed at the earlier epochs to predict the phase at $\theta_L - \theta_{\rho_o} = 2.10$.

Although this example of near-complete extinction of the field may seem pathological, it happens. The sharp phase acceleration combined with increased SNR error in the measurement is problematical for the receiver. To show this, redraw the phase prediction lines in Fig. 6-5 to run from the opposite ends of the $1-\sigma$ phase measurement error bars at $\theta_L - \theta_{\rho_o} = 2.14$ and 2.12 for the closed-loop mode and at 2.16 and 2.14 for the flywheeling mode. The worst-

case combination for this example runs from the upper end of the error bar for the earlier point to the lower end of the error bar for the later point. For these combinations, the new phase predictions at $\theta_L - \theta_{\rho_o} = 2.10$ for both the closed-loop and the flywheeling modes are more than 1/2 cycle different from the actual phase at this point. Both the closed-loop and flywheeling modes have difficulty with this example.

The receiver automatically changes to the flywheeling mode according to certain pre-set signal conditions related to SNR and measured phase residuals, typically around $\text{SNR}_v \approx 30$, and it can revert back to closed-loop tracking according to another set of conditions. But, as many of the figures in this monograph suggest, tracking in either the closed-loop or the flywheeling mode can result in cycle losses. If, for example, the earlier Doppler from the still strong and unique (m) ray in Fig. 6-2 is used in a flywheeling mode to carry the struggling receiver through the later poorer SNR conditions across a shadow zone, what happens at the contact point with the upper caustic? It depends on the strength of that caustic. A weak caustic [see Fig. 5-21(b)] reveals itself at the LEO as the envelope defining the amplitude of relatively high frequency interference fringes. There the main ray (m) is still dominant, and the frequency of the interference fringes depends on the difference in altitudes of the impact parameter of the (m) ray and the impact parameter of the caustic rays. The receiver may have difficulty tracking either one of these nascent (a) and (b) rays because of their continuing interference with the (m) ray. Figure 5-22 shows the phase acceleration spikes that result when the rays become comparable in amplitude.

On the other hand, in the examples given in Fig. 5-32 and Fig. 6-3, the extraordinary signal strength at the caustic contact is likely to induce the GPS receiver to lock onto the phase of the field there. For strong caustics, the nascent (a) and (b) rays, which are temporarily coherent in their early stage, become the principal contributors to the field at the LEO. This is the case in Fig. 6-3 at the caustic contact near $\theta_L - \theta_{\rho_o} = 2.0$. Until the impact parameters of these two nascent rays have had time to separate after the caustic contact point, there is very little interference between them. The amplitude of the field can be very strong at the LEO, depending on the curvature of the impact parameter curve θ_L vs ρ_* at the caustic contact point [see Eq. (5.12-11)]. The width of a caustic peak for strong nascent rays can be hundreds of milliseconds, roughly given by $\Delta t \sim 3 |d^2 \theta_L / d\rho_*^2|^{1/3} / \dot{\theta}_L$. This width can be several to many 20-ms correlation intervals. For examples, see Fig. 5-32 ($\Delta t \approx 150$ ms) and Fig. 6-3 ($\Delta t \approx 500$ ms). These strong and locally stable caustic fields can easily lure the GPS receiver to lock on to them. In this case, the receiver reverts from

the flywheeling mode² to closed-loop mode and takes on the Doppler of the new field formed by the composite of all the rays. In the case of Fig. 6-4, the new Doppler abruptly (<50 ms) becomes 7 Hz less than the original Doppler for the (m) ray. The (m) ray has not yet disappeared, but it is no longer “recognized.” One has a 7-Hz negative bias relative to the (m) ray, resulting from the receiver jumping from one ray to the other, from (m) to (b). However, it should be noted in this example, especially if the receiver were in fact to remain in the closed-loop mode through this delicate transition shown in Fig. 6-5, that no cycles were lost. The reported phase by the receiver in this case would be the measured phase of the complete field at the LEO from all rays. The problem is with the interpretation of the measurements resulting from the implicit adoption of a single-ray paradigm.

Probably a prudent rule of thumb declares that, whenever a caustic-like feature is encountered in the amplitude data, this probably means that it is a strong caustic in order to stand out in noisy data. This feature then is a harbinger for subsequent multipath and for the possibility that certain rays may not be properly accounted for with the usual ray theory approach, i.e., the Abel transform. In fact, the mere event of the receiver converting to the flywheeling mode should serve as an alarm announcing multipath and that spectral techniques may be required.

6.2.3 Refractivity Error from a Single-Ray Paradigm

Figure 6-6 shows the receiver in the flywheeling mode using the excess Doppler from the (m) ray just prior to entering the shadow zone ($\theta_L - \theta_{\rho_o} \approx 7$) to power through the shadow zone with poor SNR. Closed-loop operations resume with the return of strong signal near the first caustic contact point ($\theta_L - \theta_{\rho_o} \approx 2$) a few seconds later. The continued existence of the (m) and (a) rays after the (b) ray is “tracked,” and their contributions to refractivity recovery, are essentially ignored in the multipath zone with the single-ray paradigm. It is straightforward to calculate the error in recovered refractivity caused by

² For the specific refractivity profile used in Figs. 6-1 through 6-5, it is doubtful that a high-performance receiver like the BlackJack actually would drop out of the closed-loop mode upon entering the shadow zone. Diffraction softens the rate of falloff in amplitude at the shadow boundary. Also, the average minimum amplitude in this example is still 20 percent of the original amplitude. At $\theta_L - \theta_{\rho_o} \approx 2.1$, there is a single episode of almost complete cancellation between the (m) ray and the combined field from the emerging (a) and (b) rays. This event could force the receiver into the flywheeling mode, but it is somewhat irrelevant. In both modes, flywheeling or closed loop, the resulting error comes more from the analysis of the tracking data than from the receiver. Following a single-ray paradigm, the error in the refractivity recovery would be essentially the same regardless of mode.

ignoring this multipath. For example, one can adopt as the true refractivity model the same model used to generate Figs. 6-1 through 6-5. This includes an exponential model for dry air plus a localized Heaviside-like component for the water vapor layer. This causes the multipath zone shown in Fig. 6-2 with the three rays, (m), (a), and (b). The adopted model for recovery would be the exponential-only model, which has no additional Heaviside-like refractivity component and which allows no multipath. If we then extend the impact parameter curve from the (b) ray near the caustic up to the (m) ray, as shown in Fig. 6-6, we have essentially ignored the entire anomalous (a) ray and a segment of the (m) ray. These sections are shown as the dashed loop in this figure. A best fit of N_o and H from the exponential-only model to this region can be done. Comparison of the recovered refractivity profile from this fitted model with the true refractivity profile gives the error resulting from overlooking the dashed segments of the (a) and (m) rays. This is shown in Fig. 6-7. Here the true refractivity profile $N(\rho_*)$ generates the bending-angle profile shown in Fig. 6-1, but the modeled refractivity profile $\hat{N}(\rho_*)$ is only an exponential fit to the observations. This figure shows the difference in refractivity profiles between the fitted model and the true model. In this case, the error in the refractivity is negatively biased because the excess Doppler from the (b) ray, including its extrapolation backward, is on average less than the combination of the (a) and (m) rays. This systematic loss of counted cycles relative to the (m) and (a) rays is equivalent to a negative error in the Doppler, and this effectively leads in this example to a negative error in the recovered refractivity profile. See Appendix F for a further discussion of the error in recovered refractivity expressed in terms of an error in excess Doppler or bending angle.

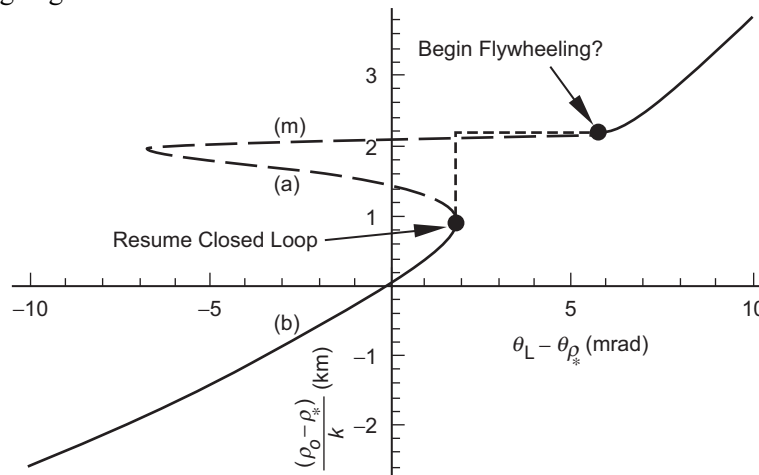


Fig. 6-6. Multipath with a single ray paradigm.

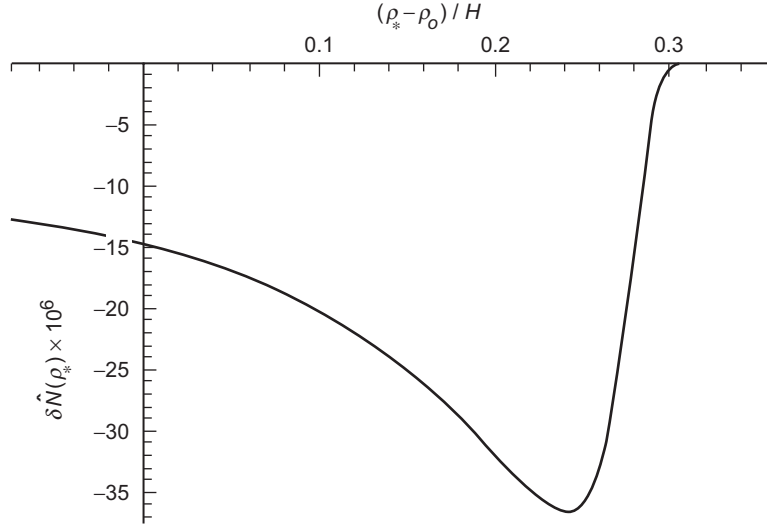


Fig. 6-7. Error in recovered refractivity $\hat{N}(\rho_*)$ as a result of ignoring the dashed sections of the (m) and (a) rays in Fig. 6-6.

An examination of actual SNR profiles from LEO occultation observations reveals a seemingly endless number of scintillation episodes, particularly as the signal passes through the water-vapor-laden lower troposphere or through various layers in the ionosphere. Flywheeling does not appear to provide a comprehensive remedy when deep scintillation occurs. The Blackjack tracking techniques probably will be augmented by JPL soon in favor of some open-loop scheme, such as reporting correlation coefficients using a realistic Doppler model, and with multiple time lags between the predicted and received time series.

6.3 Spectral Representation of the Field at the LEO

With these caveats, we now assume that an appropriate signal processing scheme has been implemented so that the amplitude and connected phase have been recovered from the receiver, plus the unavoidable SNR noise. We start from the spectral representation for an outgoing wave evaluated at the LEO located at (r_L, θ_L) . For the emitting GPS satellite located at (r_G, θ_G) with $\theta_G = \pi$, a fixed value, the spectral integral representation for the field is given from Eqs. (5.9-5) and (5.9-6), modified to account for the finite value of ρ_G . We have

$$\left. \begin{aligned} E(r_L, \theta_L) &= \frac{E_o}{\sqrt{2\pi\rho_L \sin\theta_L}} \int_0^\infty \left(\frac{\sin\theta_v^L}{\cos\theta_v^G \cos\theta_v^L} \right)^{1/2} \exp(i\Psi(+, -)) dv, \\ \Psi(+, -) &= D_v^G + D_v^L + v(\theta_v^G + \theta_v^L - \theta_L) - 2G^\dagger(v) - \frac{\pi}{4}, \\ \theta_v^G &= \sin^{-1}\left(\frac{v}{\rho_G}\right), \quad \theta_v^L = \sin^{-1}\left(\frac{v}{\rho_L}\right), \quad v < \rho_L < \rho_G, \\ D_v^G &= \sqrt{\rho_G^2 - v^2}, \quad D_v^L = \sqrt{\rho_L^2 - v^2}, \quad \rho = krn \end{aligned} \right\} \quad (6.3-1)$$

where³

³ The spectral representation for the field at the LEO when the GPS satellite is located at a finite distance, about 4.5 Earth radii, must account for the wave front curvature of the incident wave. This is a spherical wave of the form $e^{i\rho_{LG}} / \rho_{LG}$ centered at the emitting GPS satellite (see Fig. A-3). Although we did not derive this form given in Eq. (6.3-1), its extra terms compared with the form given in Eqs. (5.9-5) and (5.9-6) for the collimated case can easily be inferred from the difference in the asymptotic forms at large distances out of the atmosphere for the incoming spectral coefficients $a_i^-(\rho)$ for these two cases. These are given in Eq. (5.5-3a) for the case of a collimated or planar incident wave and in Eq. (5.5-3b) for the case of a spherical incident wave. For the latter, $a_i^-(\rho)$ carries the extra factor $i^{l+1} \xi_l^+(\rho_G) / \rho_G$, which is derived from the multipole spectral expansion for a spherical wave [5] combined with the addition theorem for spherical harmonic functions. But, for $\rho_G \gg v$, we may use the asymptotic form for the spherical Hankel function $\xi_l^+(\rho_G)$. The factor $i^{l+1} \xi_l^+(\rho_G)$ has the asymptotic form

$$i^{l+1} \xi_l^+(\rho_G) \rightarrow \left(\rho_G^2 / (\rho_G^2 - v^2) \right)^{1/4} \exp \left[i \left((\rho_G^2 - v^2)^{1/2} + v\theta_v^G \right) \right]$$

which coincides with the extra terms in Eq. (6.3-1). Here the phase delay spectral density function $\Psi(+, -)$ is referenced to the emitting GPS satellite, whereas $\Psi(+, -)$ in Eqs. (5.9-5) and (5.9-6) for the collimated case is referenced to the line $\theta = \pi/2$. Also, the constant E_o has a different meaning from E_o in Eq. (5.9-5). Essentially it must account for the $1/\rho_{LG}$ space loss that the amplitude of the spherical wave emitted from the GPS satellite incurs in traveling to the LEO. This is inconsequential in recovering the refractivity profile because it is the variability of the amplitude and phase over an occultation episode that contains the atmospheric information. The product $(\cos\theta_v^L \cos\theta_v^G)$ in Eq. (6.3.1) is related to the reduced limb distance, $D = D_G D_L / (D_G + D_L)$, with $D_G = \rho_G \cos\theta_{\rho^*}^G$ and $D_L = \rho_L \cos\theta_{\rho^*}^L$.

The ray theory interpretation of θ_v^L and θ_v^G is as follows. Let $v = v^*$ be a spectral number at which Ψ assumes a stationary value. When super-refracting situations are avoided, we know that to high accuracy $v^* \doteq \rho_*$, the impact parameter of the

$$\left. \begin{aligned} 2G^\dagger(\nu) &\doteq 2 \int_{\rho^\dagger}^{\infty} \frac{d \log n}{d \rho} g(\hat{y}) d\rho \doteq - \int_{\nu}^{\infty} \alpha_L(\omega) d\omega, \\ g(\hat{y}) &= \pi K_v^2 \left(\text{Ai}'[\hat{y}]^2 + \text{Bi}'[\hat{y}]^2 - \hat{y} (\text{Ai}[\hat{y}]^2 + \text{Bi}[\hat{y}]^2) \right), \\ \hat{y} &\doteq \frac{1}{4K_v^4} (\nu^2 - \rho^2), \quad K_x = \left(\frac{x}{2} \right)^{1/3}, \\ \nu &= l + \frac{1}{2}, \quad \rho^\dagger = \nu - \hat{y}^\dagger K_{\rho^\dagger}, \quad \hat{y}^\dagger = 0.44133 \dots \end{aligned} \right\} \quad (6.3-2)$$

The spectral density function $G^\dagger(\nu) = G[\rho^\dagger(\nu), \nu]$ for the phase delay from the refractive gradient and $\rho^\dagger(\nu)$ are discussed more fully in Section 5.7, and their forms are given in Eqs. (5.7-2) and (5.7-11), respectively.⁴ They are the spectral density forms applicable to an outgoing wave at the position of the LEO. We have taken minor license with Eq. (5.9-5) by consolidating the radial and transverse components into a single scalar form for the electric field $E(r_L, \theta_L)$. The resulting error is negligible for occultations.

We note that the spectral density for the phase, $\Psi(+, -)$, is a function of $(\rho_G, \rho_L, \theta_L, \nu)$. $\Psi(+, -)$ is the appropriate spectral density function for a position located well into the upper half-plane, $\pi \gg \theta_L \gg 0$, and in the outgoing quadrant, $\pi/2 - \alpha_L \gg \theta_L \gg 0$. $\Psi(+, -)$ gives the spectral density of the complete phase delay at the LEO position (r_L, θ_L) relative to the emitting GPS satellite located at (r_G, θ_G) with $\theta_G = \pi$. It includes the geometric delay terms and the term $-2G^\dagger(\nu)$ for the delay from the refractive gradient (see Fig. 1-14). The geometric delay term, D_v^L , gives the delay in phase along a straight line between the LEO and the tangency point of the line on a sphere of radius $\nu < \rho_L$ centered at the origin. The term $\nu(\theta_L - \theta_v^L)$ is an arc length along this sphere of radius ν , and it is subtracted from D_v^L to correct it to the intersection of the sphere with the line $\theta = \pi/2$, which is the fixed reference line for computing phase delays at the LEO. Similarly, the terms $D_v^G + \nu\theta_v^G$ give the geometric phase delay from the emitting GPS satellite along the straight line

corresponding ray. Then from Eq. (6.3-1) and Bouguer's law, it follows that $\theta_{\rho^*}^L$ becomes the angle between the ray path tangent vector and the radius vector of the LEO, $\chi_L + \delta_L$, in Fig. A-3. Similarly, $\theta_{\rho^*}^G \rightarrow \chi_G + \delta_G$. Note that, from Fig. A-3 with $\theta_G = \pi$, it follows that $\theta_{\rho^*}^G + \theta_{\rho^*}^L - \theta_L \rightarrow \delta_G + \delta_L = \alpha_L$.

⁴ Incidentally, the difference between $\rho^\dagger(\nu)$ and ν is very small for a large sphere, $r_o/\lambda \gg 1$. Here that spatial difference is about 7 m.

to the tangency point on the sphere of radius ν and thence along the sphere to the line $\theta = \pi/2$. For the LEO located at a given point (r_L, θ_L) , the spectral neighborhoods around the stationary phase points ν^* , that is, where $\partial\Psi/\partial\nu|_{\nu^*} = 0$, provide the principal contributions to this spectral integral in Eq. (6.3-1).

$E(r_L, \theta_L)$ is the scalar field at the LEO; the phase of $E(r_L, \theta_L)$ includes an integer multiple of 2π driven by the absolute phase represented by the spectral density function $\Psi(+, -)$. But, as we just discussed, it is problematic whether or not the actual phase measurements can yield unambiguous connected phase at all times. Nevertheless, it is important to have the correct phase change between observation epochs, uncorrupted by systematic cycle slipping by the receiver or by the post-measurement data editing. Occasional cycle breaks, although undesirable, are probably inevitable. We assume here that cycle breaks have been fixed.

6.3.1 Stopped Field at the LEO

Let $\hat{E}(r_L, \theta_L)$ be defined as the “stopped” or “counter-rotated” signal received by the LEO. In this case, “stopped” means that the orbital Doppler tone between the LEO and the observed GPS satellite has been removed. Also, the excess Doppler based on a first-order model for the atmospheric refractivity signature has been removed. Thus,

$$\hat{E}(r_L, \theta_L) = E(r_L, \theta_L) \exp(-i\phi_m(t)) \quad (6.3-3)$$

where the model phase $\phi_m(t)$ is a known function that describes the time history of the stopping phase. Dealing with $\hat{E}(r_L, \theta_L)$ rather than $E(r_L, \theta_L)$ alleviates aliasing problems in finite sampling techniques and sharpens the resolution. To get an idea of the magnitude of the variability of $\phi_m(t)$, we will form the time derivative of $\Psi(+, -)$, the spectral density for the phase delay at the LEO, given in Eq. (6.3-1). We evaluate Ψ at a stationary point in spectral number $\nu^* \doteq \rho_*$, where $\partial\Psi/\partial\nu = \theta_\nu - \theta_L - 2dG^\dagger/d\nu = 0$, and then we differentiate it with respect to time to obtain $\dot{\Psi}_*$. This already has been discussed in Section 5.12 for a circular LEO orbit with a coplanar geometry, that is, with the GPS satellite located in the orbit plane of the LEO.

6.3.2 The Obliquity Factor

However, we also should allow for the obliquity effect because in general coplanarity does not apply. From Fig. 6-8, we have two angles, θ_L and $\tilde{\theta}_L$ defining the angular position of the LEO. Here θ_L gives the angular position in

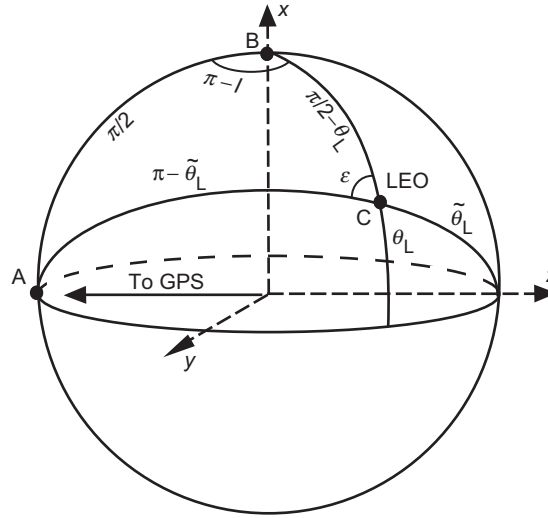


Fig. 6-8. A spherical geometry for non-coplanar LEO and GPS orbits. GPS satellite is located infinitely afar along the negative z-axis.

the LEO orbit plane, but $\tilde{\theta}_L$ gives it in the propagation plane, which is defined by the ray from the GPS satellite located in the negative z-direction⁵ to the LEO. This propagation plane includes the “geocenter” (the center for the local geoid) and defines the great circle arc AC on the unit sphere in Fig. 6-8. The LEO orbit plane defines the great circle arc BC. The departure from coplanarity is given by the inclination angle I of the LEO orbit plane about the x-axis in the figure relative to the direction to the GPS satellite. The inclination angle I is satellite-position dependent, but it is readily expressed in terms of the orbit elements for the two satellites. The boresight-offset angle is ε . This is the azimuthal angle about the radial axis relative to the in-orbit plane direction at which the GPS satellite would be seen from the LEO. The spherical triangle ABC in Fig. 6-8 gives the relationship between θ_L and $\tilde{\theta}_L$. We have

⁵ We assume here for calculation of the obliquity factor that the emitting GPS satellite is located infinitely afar in the negative z-direction, $\theta_G = \pi$.

$$\left. \begin{aligned} \sin \varepsilon &= \frac{\sin I}{\sin \tilde{\theta}_L}, \quad \tan \tilde{\theta}_L = \tan \theta_L \cos \varepsilon, \\ \cos \tilde{\theta}_L &= \cos \theta_L \cos I, \\ \frac{d\tilde{\theta}_L}{d\theta_L} &= \cos^2 I \cos \varepsilon = \frac{\cos^2 I}{\sin \tilde{\theta}_L} \sqrt{\sin^2 \tilde{\theta}_L - \sin^2 I} \end{aligned} \right\} \quad (6.3-4)$$

This provides the relationships between θ_L and $\tilde{\theta}_L$, as well as the obliquity factor $d\tilde{\theta}_L / d\theta_L$ to reduce the Doppler for the effect of non-coplanarity. It follows that

$$\dot{\tilde{\theta}}_L = \left(\frac{d\tilde{\theta}_L}{d\theta_L} \right) \dot{\theta}_L \quad (6.3-5)$$

This obliquity factor is essentially constant over an occultation episode; thus, the relationship between $\tilde{\theta}_L$ and θ_L is essentially linear. The obliquity factor is shown in Fig. 6-9 as a function of I . Here $\tilde{\theta}_{L_o} = \sin^{-1}(r_o / r_L)$ with $r_L / r_o = 1.1$, which gives about the correct value of $\tilde{\theta}_L$ during an occultation. Thus, an inclination of 30 deg reduces the excess Doppler to about two-thirds of the coplanar value. It is $\tilde{\theta}_L$ that should be used in Bouguer's law and in the spectral density functions involving phase. Accordingly, we adopt the following convention in the subsequent discussion. In any expression that involves a sensitive variable, such as phase or angular velocity, we shall replace θ_L with $\tilde{\theta}_L$; otherwise, we leave the notation as is.

6.3.3 Doppler Variability

We now estimate the variability of $\varphi_m(t)$. For the purpose of calculating the Doppler variability, we assume circular orbits for the satellites. From Eq. (5.12-4), it follows after this replacement of θ_L with $\tilde{\theta}_L$ in Bouguer's law that

$$\dot{\Psi}_* \doteq -\rho_* \dot{\tilde{\theta}}_L \quad (6.3-6)$$

where the phase $\Psi_* = \Psi(\rho_G, \rho_L, \tilde{\theta}_L, \rho_*)$, and ρ_* is the impact parameter corresponding to a specific ray, not necessarily unique. To simplify this calculation, we assume that the emitting GPS satellite is at an infinite distance. Its actual finite distance and orbital motion have a minor effect on our estimate

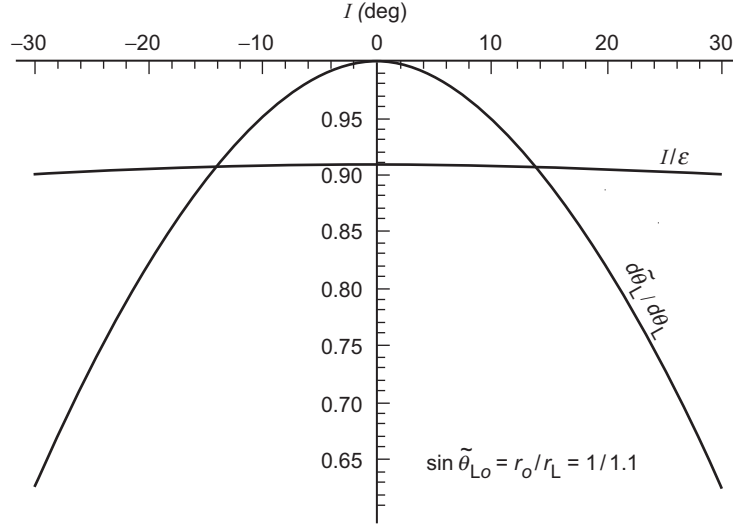


Fig. 6-9. Obliquity factor $d\tilde{\theta}_L/d\theta_L$ and I/ε versus LEO orbit plane inclination angle I .

here. From Bouguer's law in Eq. (5.6-5) for the GPS satellite at an infinite distance, we have

$$\rho_* = \rho_L \sin(\tilde{\theta}_L + \alpha_L) = \rho_o + D_L \alpha_L + O[\alpha_L^2] \quad (6.3-7)$$

where $\rho_o = \rho_L \sin \tilde{\theta}_L$ and $D_L = \rho_L \cos(\tilde{\theta}_L + \alpha_L)$. The quantity D_L is close to the distance (or reduced distance) in phase units (i.e., distance $\times 2\pi/\lambda$) from the LEO to the Earth's limb, even with a modest cosine effect from orbit inclination angle I factored in. For the 20-cm wavelength of the GPS signal, $\rho_o \approx 2 \times 10^8$ at sea level, and for a LEO orbit radius $r_L = 1.1r_o$, $D_L \approx 1 \times 10^8$. It follows that

$$\dot{\Psi}_* \doteq -\rho_o \dot{\tilde{\theta}}_L - (D_L \dot{\tilde{\theta}}_L) \alpha_L \quad (6.3-8)$$

The first term on the right-hand side (RHS) of Eq. (6.3-8) produces the orbital Doppler term due to the LEO. For a typical LEO orbit, $\dot{\tilde{\theta}}_L \approx 1$ mrad/s, and it is essentially constant with time; thus, for the LEO part, $\rho_o \dot{\tilde{\theta}}_L / 2\pi \approx 30$ kHz times the obliquity factor $d\tilde{\theta}_L/d\theta_L$, which is shown in Fig. 6-9 as a function of the inclination angle I of the LEO orbit plane.

The orbital velocity of a GPS satellite is about half the LEO velocity because its orbit radius is about four times larger. During an occultation, the position of a GPS satellite is located about 4.5 Earth radii away from the LEO

on the far side of the Earth; so, only about a quarter of its velocity vector projects plus or minus in the direction of the LEO. Also, the GPS satellite orbit planes are inclined differently to the LEO orbit plane, and the limb of the Earth as seen from the LEO is offset downward from the LEO orbit velocity direction by roughly 25 deg. The upshot is that all of these factors combine to yield a maximum Doppler during an occultation from both LEO and GPS orbital kinematics of around 35 kHz.

The second term in Eq. (6.3-8) is the excess Doppler from the bending angle α_L caused by the atmospheric refractivity; here $D_L \dot{\tilde{\theta}}_L / 2\pi \approx 15(d\tilde{\theta}_L / d\theta_L)$ Hz/mrad. Dry air yields a bending angle for a ray path tangency point at sea level of about 20 mrad; so, this component reaches about 300 Hz. But, bending angles through water vapor in the lower troposphere can exceed twice this level. The water vapor contribution is largely unknown a priori, but it can be characterized statistically by latitude and season. Excess Doppler signatures typically range over several hundred hertz.

What about the variability of these Doppler frequencies? Let us assume that the LEO is in a circular orbit. Then from Eq. (6.3-6) it follows that

$$\ddot{\Psi}_* \doteq -\dot{\rho}_* \dot{\tilde{\theta}}_L \quad (6.3-9)$$

The term $\rho_* \ddot{\tilde{\theta}}_L \ll \dot{\rho}_* \dot{\tilde{\theta}}_L$, and it is ignored here. The acceleration contribution from the GPS satellite will be small over the relatively short time intervals of interest here. Upon differentiating ρ_* from Bouguer's law in Eq. (6.3-7), it follows that

$$\dot{\rho}_* = D_L \dot{\tilde{\theta}}_L \zeta_L \quad (6.3-10)$$

where $\zeta_L = (1 - D_L d\alpha_L / d\rho_*)^{-1}$ is the defocusing factor. It follows that the acceleration in the phase term is given by

$$\ddot{\Psi}_* \doteq -D_L \dot{\tilde{\theta}}_L^2 \zeta_L \quad (6.3-11)$$

Similarly, it follows that the acceleration from the orbital motion of the LEO is given by

$$\frac{d^2 D_L}{dt^2} \doteq D_L \dot{\tilde{\theta}}_L^2 \quad (6.3-12)$$

Subtracting Eq. (6.3-12) from Eq. (6.3-11) gives the acceleration in excess phase:

$$2\pi\dot{f}_D = \ddot{\Psi}_* - \frac{d^2 D_L}{dt^2} \doteq -D_L^2 \ddot{\theta}_L^2 \frac{d\alpha_L}{d\rho_*} \zeta_L \xrightarrow{\alpha'_L \rightarrow -\infty} D_L \ddot{\theta}_L^2 \quad (6.3-13)$$

It follows for strong defocusing that the excess Doppler rate approaches a constant value with time, 10 to 15 Hz/s, depending on the obliquity of the orbit and propagation planes. (Therefore, the bending angle rate of a given ray in strong defocusing conditions will approach a constant, $d\alpha_L / dt \rightarrow \sim 1$ mrad/s, or, equivalently, $d\alpha_L / d\tilde{\theta}_L \rightarrow \sim 1$.)

Over the course of a few tens of seconds that we will be interested in recovering the refractivity profile under adverse signal conditions, how well can we fit the stopping phase with a simple linear polynomial in time, $\phi_m(t) = \omega_m t$? Equation (6.3-13) suggests that in strong defocusing this linear form should be good. We set $\omega_m = \dot{\Psi}_*$. Then $\dot{\Psi} - \dot{\phi}_m(t) \approx \ddot{\Psi}_* t$. From Eq. (6.3-11), it follows that $\ddot{\Psi}_* / 2\pi < \sim 2$ Hz/s in the lower troposphere where the defocusing factor from dry air has a value around 1/10. The defocusing in the lower troposphere causes the impact parameter separations between multipath rays to be proportionately compressed, thereby reducing their Doppler differences by a factor of about 10. Thus, for a 10-s single-sided sample interval, we can use a linear term in time to stop the Doppler in the signal with a frequency runoff of a few tens of hertz. Sampling the signal at a 50-Hz rate usually should satisfy the Nyquist criterion for this sample interval. At the altitude of the sporadic E-layer, the ambient value of the defocusing factor is essentially unity; we would need a narrower sample interval there.

The last question concerns the spread in Doppler tones from different multipath rays. We already have seen that the spread in altitudes of the tangency points typically is less than 5 km. Thus, the maximum spread in Doppler is less than $(D_L \dot{\theta}_L / 2\pi)(5k / D_L) \approx 25$ Hz; the bandwidth of most interference spectra is less than 10 Hz. A sample rate of 50 Hz should suffice.

Incidentally, Eq. (6.3-10), which gives the velocity of the impact parameter of a ray, shows the retardation caused by the defocusing factor ζ_L . In the lower troposphere, the dry air component of the defocusing systematically compresses the altitude separation between multipath rays and narrows the maximum bandwidth of the interference spectrum; see Eq. (5.12-18).

6.4 Refractivity Recovery

Let us apply a discrete Fourier transform to the stopped LEO observations given in Eq. (6.3-3) and to the spectral representation for the stopped wave given in Eq. (6.3-1). For the latter, we have

$$\left. \begin{aligned} \hat{E}[\omega] &= \sum_{k=-M/2}^{M/2} \hat{E}(r_L, \theta_L(t_k)) \exp\left(i\omega \frac{kT}{M}\right), \\ \tilde{\theta}_L(t_k) &= \tilde{\theta}_{Lo} + \dot{\tilde{\theta}}_L(t_k - t_o) = \tilde{\theta}_{Lo} + \dot{\tilde{\theta}}_L \frac{kT}{M}, \quad \theta_G \equiv \pi \end{aligned} \right\} \quad (6.4-1)$$

Here $\tilde{\theta}_{Lo} = \tilde{\theta}_L(t_o)$ is the LEO orbit angle at the center of the data interval measured in the plane of incidence; see Fig. 6-8. Equation (6.3-4) provides the relationship between $\tilde{\theta}_L$ and θ_L . T is the total time span covered by the observations, and $M+1$ is the total number (odd) of samples; for example, $M=50T$ for a 50-Hz sample rate. Using the spectral representation in Eq. (6.3-1) for $\tilde{E}(r_L, \theta_L)$ and $\varphi_m(t) = \omega_m(t - t_o)$ for the stopping phase, from Eq. (6.4-1) we have

$$\left. \begin{aligned} \hat{E}[\omega] &= \sum_{k=-M/2}^{M/2} \hat{E}(r_L, \theta_L(t_k)) e^{i\omega \frac{kT}{M}} \\ &= \sum_{k=-M/2}^{M/2} e^{i(\omega - \omega_m) \frac{kT}{M}} \left(\frac{E_o}{\sqrt{2\pi\rho_L \sin \tilde{\theta}_{Lk}}} \int_0^\infty \left(\frac{\sin \tilde{\theta}_v^L}{\cos \tilde{\theta}_v^G \cos \tilde{\theta}_v^L} \right)^{1/2} e^{i\Psi_L} dv \right) \\ &\doteq \frac{E_o e^{i\Psi_{Lo}}}{\sqrt{2\pi\rho_L \sin \tilde{\theta}_{Lo}}} \int_0^\infty \left(\frac{\sin \tilde{\theta}_v^L}{\cos \tilde{\theta}_v^G \cos \tilde{\theta}_v^L} \right)^{1/2} \left(\sum_{k=-M/2}^{M/2} e^{ik(\omega - \omega_m - v\dot{\tilde{\theta}}_L) \frac{T}{M}} \right) dv, \\ \Psi_{Lo} &= D_v^G + D_v^L + v(\tilde{\theta}_v^G + \tilde{\theta}_v^L - \tilde{\theta}_{Lo}) - 2G^\dagger(v) - \frac{\pi}{4} \end{aligned} \right\} \quad (6.4-2)$$

Now we replace the discrete Fourier transform with the integral transform using the fact that

$$\sum_{k=-M/2}^{M/2} \exp(iuk) = \frac{\sin((M+1)u/2)}{\sin(u/2)} \xrightarrow{M \rightarrow \infty} 2\pi\delta(u), \quad -\pi \leq u \leq \pi \quad (6.4-3)$$

Here $\delta(u)$ is the Dirac delta function. Setting $u = \pi$ defines the Nyquist limit, $|\omega| \leq \pi M/T$. Upon replacing the discrete “delta function” in Eq. (6.4-2) with the Dirac delta function, it follows that the Fourier transform of $\tilde{E}(r_L, \theta_L)$ is given by

$$\left. \begin{aligned} \hat{E}[\omega_v] &= 2\pi E_o \sqrt{\frac{1}{2\pi\rho_L \sin \tilde{\theta}_{Lo}}} \left(\frac{\sin \tilde{\theta}_v^L}{\cos \tilde{\theta}_v^G \cos \tilde{\theta}_v^L} \right)^{1/2} \exp(i\Psi_{Lo}), \\ \Psi_{Lo} &= D_v^G + D_v^L + v(\tilde{\theta}_v^G + \tilde{\theta}_v^L - \tilde{\theta}_{Lo}) - 2G^\dagger(v) - \frac{\pi}{4}, \\ \omega_v &= \omega_m + \dot{\tilde{\theta}}_L v, \quad D_v^G = \sqrt{\rho_G^2 - v^2}, \quad D_v^L = \sqrt{\rho_L^2 - v^2} \end{aligned} \right\} \quad (6.4-4)$$

For a finite sample interval, the discrete Fourier transform yields the discrete delta function, which has the $\sin Nx / \sin x$ character shown in Eq. (6.4-3), and the actual time series would have additive noise. The granularity threshold from the discrete transform can be obtained from the first zero of the discrete delta function in Eq. (6.4-3), which occurs at $u = 2\pi / (M + 1)$. This is equivalent to $\Delta\omega = 2\pi / T$, which is essentially the uncertainty inequality for a discrete process. In impact parameter space, this relationship maps into a granularity in altitude of $\lambda\Delta\rho_* / 2\pi = \lambda\dot{\tilde{\theta}}_L^{-1}\Delta\omega / 2\pi = \lambda / (\dot{\tilde{\theta}}_L T) \approx 200 / T$ m, or about 20 m for $T = 10$ s. Instead of a Fourier transform, one could use any one of several other transform schemes, such as the Morlet wavelet transform, which treats the time series as a spectral composition of wave packets. The subsequent equations will differ, and their efficiencies in recovering the refractivity profile might vary, but recovery should still be feasible. For the purpose of outlining this particular spectral approach for recovering the refractivity profile, we avoid further discussion of these important computational and related stochastic issues.

Note in Eq. (6.4-4) that $\omega_m \sim 2 \times 10^5$ rad/s, or 30 to 35 kHz. On the other hand, $\omega_v / 2\pi$ varies over only a few tens of hertz within the time interval for which the Fourier transform is applied. We have used the slowly varying character of $\tilde{\theta}_v^L$ and $\tilde{\theta}_v^G$ to simplify the spectral expressions given in Eq. (6.4-4). Over the bandwidth spanned by ω_v , $\tilde{\theta}_v^L + \tilde{\theta}_v^G$ changes by less than 0.1 percent. Thus, we may set $\tilde{\theta}_v^L + \tilde{\theta}_v^G = \tilde{\theta}_{Lo} + \alpha_{Lo} \doteq \tilde{\theta}_{Lo}$ in the slowly varying terms (but not in Ψ_{Lo}). The error here is roughly 1 percent or smaller, the ratio $\alpha_L(t_k) / \tilde{\theta}_L(t_k)$. The Fourier transform in Eq. (6.4-4) further simplifies to

$$\left. \begin{aligned} \hat{E}[\omega_v] &= 2\pi E_o \sqrt{\frac{1}{2\pi D}} \exp(i\Psi_{Lo}), \\ \Psi_{Lo} &= D_v^G + D_v^L + v(\tilde{\theta}_v^G + \tilde{\theta}_v^L - \tilde{\theta}_{Lo}) - 2G^\dagger(v) - \frac{\pi}{4}, \\ \omega_v &= \omega_m + \dot{\tilde{\theta}}_L v, \quad D^{-1} = D_L^{-1} + D_G^{-1} \end{aligned} \right\} \quad (6.4-5)$$

We now take the Fourier transform over the occultation sequences of stopped phase and amplitude measurements made by the LEO, given in Eq. (6.3-3). The temporal breadth of this sequence T would depend on one's goals for refractivity recovery. We equate these two Fourier transforms. The left-hand side (LHS) on the upper line of Eq. (6.4-5) becomes the Fourier transform of the sampled amplitude and stopped phase of the field measured by the LEO; the RHS is from wave theory.

We note the one-to-one correspondence between ω_v or excess Doppler and the spectral number v in wave theory, or the impact parameter in ray optics, which holds when spherical symmetry applies. Also, we note that the bending angle may not be a unique function of time (or $\tilde{\theta}_L$), but it is a unique function of excess Doppler, and when spherical symmetry holds it is a unique function of impact parameter through Bouguer's law. The impact parameter diagrams in Figs. 5-20, 5-26, 5-28, 5-31, and 6-2 all show implicitly this uniqueness property of the bending angle versus impact parameter when spherical symmetry holds. See also Eqs. (6.3-6) and (6.3-8), which apply to a circular LEO orbit. We have converted through a Fourier transform the time series of phase and amplitude measurements of the field, in which the bending angle may not be unique, into a spectral series in which the bending angle is unique (when spherical symmetry applies). It follows that we should be able to unambiguously determine the bending-angle profile versus excess Doppler from the Fourier transform $\hat{E}[\omega]$, given, of course, the limitations imposed by measurement errors.

Returning to Eq. (6.4-5), the LHS is the Fourier transform $\hat{E}[\omega]$ from the observations. It is a known quantity. The RHS is from wave theory; it also contains quantities that are known a priori or from POD information, except for $G^\dagger(v) = G[\rho^\dagger(v), v]$. Forcing equality between these two Fourier transforms forces the phase of $\hat{E}[\omega]$ to equal Ψ_{Lo} . Therefore, we can determine values for $G^\dagger(v)$ from Eq. (6.4-5) over the Fourier bandwidth spanned by ω .

However, a more suitable platform for extracting values for $\log n$ is $dG^\dagger(v)/dv$. Recalling that $g(\hat{y}^\dagger) = 0$, it follows from Eq. (6.3-2) that

$$\frac{dG^\dagger}{dv} \doteq -\pi K_{v_\omega} \int_{\rho^\dagger}^{\infty} \frac{d \log n}{d\rho} (\text{Ai}[\hat{y}]^2 + \text{Bi}[\hat{y}]^2) d\rho \quad (6.4-6)$$

Let us now differentiate the Fourier transforms in Eq. (6.4-5) with respect to ω . Noting that $d\omega_v/dv = \dot{\tilde{\theta}}_L$, we obtain

$$\frac{d \log \hat{E}[\omega_v]}{d\omega_v} = i \left(\tilde{\theta}_v - \tilde{\theta}_{Lo} - 2 \frac{dG^\dagger}{dv} \right) \dot{\tilde{\theta}}_L^{-1} \quad (6.4-7)$$

However, from Eq. (6.4-1), it follows that

$$\frac{d}{d\omega}(\hat{E}[\omega]) = i \int_{-\infty}^{\infty} t \hat{E}(\rho_L, \theta_L(t)) \exp(i\omega t) dt \quad (6.4-8)$$

No explicit differentiation of the observed phase and amplitude with respect to time is required to obtain the derivative of $\hat{E}[\omega]$ with respect to ω . In Eq. (6.4-6), we note that $\partial(\partial G[\rho, v]/\partial v)/\partial \rho \neq 0$ at $\rho = \rho^\dagger(v)$ (whereas $\partial G[\rho, v]/\partial \rho = 0$). It follows that Eq. (6.4-6) provides a stable means for determining the profile for $d \log n / d\rho$ from the determination of $dG[\rho^\dagger(v), v]/dv$.

Let the Fourier observation function $F[\omega]$ be defined by

$$\dot{\theta}_L F[\omega_v] = i \dot{\theta}_L \frac{d \log \hat{E}[\omega_v]}{d\omega_v} + (\tilde{\theta}_{v_\omega} - \tilde{\theta}_{L_o}) \quad (6.4-9)$$

$F[\omega_v]$ is a determined spectral quantity from the measurements and the POD information. From Eqs. (6.4-6) through (6.4-11), it follows that

$$\left. \begin{aligned} -2\pi K_v \int_{\rho^\dagger}^{\infty} \frac{d \log n}{d\rho} (\text{Ai}[\hat{y}]^2 + \text{Bi}[\hat{y}]^2) d\rho &= 2 \frac{dG^\dagger(v)}{dv} = \dot{\theta}_L F[\omega_v] \\ \rho^\dagger = v - \hat{y}^\dagger K_v &= \frac{\omega_v - \omega_m}{\dot{\theta}_L} - \hat{y}^\dagger K_v \end{aligned} \right\} \quad (6.4-10)$$

Equation (6.4-10) is in effect a linear system, an integral equation from which the profile $d \log n / d\rho$ may be recovered from a spectral sequence of known values for $F[\omega]$ based on the spectral derivative of the Fourier transform of the observations. Recalling Eqs. (5.4-3) and (3.8-7), the negative argument asymptotic forms for the Airy functions are $\text{Ai}[\hat{y}]^2 + \text{Bi}[\hat{y}]^2 \rightarrow \pi^{-1}(-\hat{y})^{-1/2}$ with $\hat{y} \doteq K_v^{-4}(v^2 - \rho^2)/4$. Equation (6.4-10) becomes

$$\begin{aligned} -2\pi K_v \int_{\rho^\dagger}^{\infty} \frac{d \log n}{d\rho} (\text{Ai}[\hat{y}]^2 + \text{Bi}[\hat{y}]^2) d\rho &\rightarrow \\ -2v \int_v^{\infty} \frac{d \log n}{d\rho} \frac{d\rho}{\sqrt{\rho^2 - v^2}} &= \alpha_L(v) \end{aligned} \quad (6.4-11)$$

It follows from Eqs. (6.4-10) and (6.4-11) that

$$\left. \begin{aligned} \alpha_L(v) &\leftrightarrow F[\omega_v] \dot{\tilde{\theta}}_L \\ \omega_v &= \omega_m + \dot{\tilde{\theta}}_L v \end{aligned} \right\} \quad (6.4-12)$$

To the extent to which the asymptotic forms for the Airy functions are applicable, $F[\omega_v]$ is proportional to the bending angle for an impact parameter value of v . It follows for a setting occultation ($\dot{\tilde{\theta}}_L < 0$) that, if $\alpha_L(v) \rightarrow 0$, $v \rightarrow \infty$, then $F[\omega_v] \rightarrow 0$, $\omega_v \rightarrow -\infty$.

More generally, setting $v = \rho_*$, corresponding to a value of $\omega_v = \omega_m - \rho_* |\dot{\tilde{\theta}}_L|$ within the Fourier bandwidth, one can form

$$\left. \begin{aligned} &\int_{v^\dagger}^{\infty} \frac{\dot{\tilde{\theta}}_L F[\omega_v]}{\sqrt{v^2 - \rho_*^2}} dv = \\ &-2\pi \int_{v^\dagger}^{\infty} \frac{K_v dv}{\sqrt{v^2 - \rho_*^2}} \left(\int_{\rho^\dagger}^{\infty} \frac{d \log n}{d\rho} (\text{Ai}[\hat{y}]^2 + \text{Bi}[\hat{y}]^2) d\rho \right) \\ &= -2\pi \int_{\rho_*}^{\infty} \frac{d \log n}{d\rho} \left(\int_{\rho_*}^{\rho} \frac{(\text{Ai}[\hat{y}]^2 + \text{Bi}[\hat{y}]^2)}{\sqrt{v^2 - \rho_*^2}} K_v dv \right) d\rho \\ &= \pi \int_{\rho_*}^{\infty} \log n(\rho) W(\rho, \rho_*) d\rho, \quad v^\dagger = \rho_* + \hat{y}^\dagger K_{\rho_*}, \quad \rho^\dagger = v - \hat{y}^\dagger K_v \end{aligned} \right\} \quad (6.4-13)$$

The second integral on the third line involving the Airy functions is completely deterministic. The fourth line is obtained from integrating by parts. The weighting function $W(\rho, \rho_*)$ is given by

$$\left. \begin{aligned} &W(\rho, \rho_*) = \\ &2K_\rho \frac{\text{Ai}[0]^2 + \text{Bi}[0]^2}{\sqrt{\rho^2 - \rho_*^2}} - 4 \int_{\rho_*}^{\rho} \frac{\text{Ai}[\hat{y}] \text{Ai}'[\hat{y}] + \text{Bi}[\hat{y}] \text{Bi}'[\hat{y}]}{\sqrt{v^2 - \rho_*^2}} K_v^2 dv, \\ &\int_{\rho_*}^{\rho} W(\rho, \rho_*) d\rho = 2 \int_{\rho_*}^{\rho} \frac{\text{Ai}[\hat{y}]^2 + \text{Bi}[\hat{y}]^2}{\sqrt{v^2 - \rho_*^2}} K_v dv \xrightarrow{\rho \rightarrow \infty} 1, \\ &\hat{y} \doteq \frac{1}{4K_v^4} (v^2 - \rho^2) \end{aligned} \right\} \quad (6.4-14)$$

In the limit as $\lambda \rightarrow 0$, $W(\rho, \rho_*)$ resembles a Dirac delta function, having similar properties. $W(\rho, \rho_*)$ and its integral, which rapidly approaches unity

with increasing $\rho > \rho_*$, are shown in Fig. 6-10. The decay profile of $W(\rho, \rho_*)$ is determined by the span in \hat{y} space over which the Airy functions make their transition to negative argument asymptotic forms, $\sim 2k^{-1}K_{\rho_*} = 2(\lambda^2 n_* r_* / 4\pi^2)^{1/3} \approx 30$ m. Therefore, $W(\rho, \rho_*)$ strongly weights the contribution from $\log n(\rho)$ in the convolution integral in Eq. (6.4-13) at $\rho = \rho_*$, and it attenuates rapidly for $\rho > \rho_*$ to nearly zero within 30 m. The half-area point is at 7 m. This spatial interval, $\sim 2(\lambda^2 n_* r_* / 4\pi^2)^{1/3}$, is where the differences between wave theory and ray theory mainly arise. If we approximate $W(\rho, \rho_*)$ by a Dirac delta function, we have

$$\frac{1}{\pi} \int_{v^\dagger(\rho_*)}^{\infty} \frac{\dot{\theta}_L F[\omega_v]}{\sqrt{v^2 - \rho_*^2}} dv = \int_{\rho_*}^{\infty} \log n(\rho) W(\rho, \rho_*) d\rho \rightarrow \log n(\rho_*) \quad (6.4-15)$$

Equation (6.4-15) is the wave theory equivalent of the Abel integral transform. The Abel transform owes its existence to a remarkable property of the integral,

$$\int_a^b \frac{2x dx}{\sqrt{(x^2 - a^2)(b^2 - x^2)}} = \pi \quad (6.4-16)$$

for all real positive values of a and $b > a$. Unfortunately, there does not seem to be the crisp equivalent of the Abel transform in wave theory. From

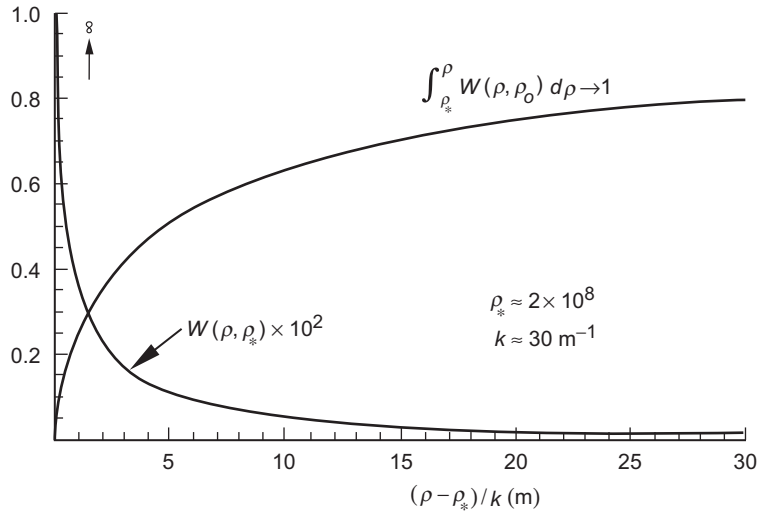


Fig. 6-10. Weighting function $W(\rho, \rho_*)$ in the wave theory analog of the Abel transform.

Eq. (6.4-13) and upon setting the Airy functions to their negative argument asymptotic forms, $\text{Ai}[\hat{y}]^2 + \text{Bi}[\hat{y}]^2 \rightarrow \pi^{-1}(-\hat{y})^{-1/2}$, we have

$$2\pi \int_{\rho_*}^{\rho} \frac{(\text{Ai}[\hat{y}]^2 + \text{Bi}[\hat{y}]^2)}{\sqrt{v^2 - \rho_*^2}} K_v dv \rightarrow \int_{\rho_*}^{\rho} \frac{2v dv}{\sqrt{(v^2 - \rho_*^2)(\rho^2 - v^2)}} = \pi \quad (6.4-17)$$

By solving the convolution integral in Eq. (6.4-15), the refractivity profile is recovered from an integral operation on the spectral quantity $F[\omega_v]$, which is related directly to the spectral derivative of the Fourier transform of the stopped observations $\hat{E}(r_L, \theta_L(t))$ through Eqs. (6.3-3) and (6.4-9), and which is essentially proportional to the bending angle associated with an impact parameter value v .

The time span T used in the Fourier treatment just described has not been specified. When the SNR permits, one can partition the entire data set into a time-ordered series of contiguous subsets or data packets of temporal width ΔT_k . Over each packet, a Fourier transform can be applied, and the spectrum for each of these strips can be assembled contiguously and displayed as a function of time, or as a function of nominal ray path tangency altitude, and so on. Figure 1-11, which is from [6], shows an example of this approach. This is one example of the so-called sliding spectrum technique [7].

6.4.1 Super-Refractivity

The integral for $2dG^\dagger(v)/dv$ in terms of the refractivity gradient in Eq. (6.4-6) requires special treatment to handle super-refractivity conditions. We have used $\rho = knr$ as the integration variable for convenience, but implicit in its use is the assumption that $d\rho/dr$ is positive throughout. Within a super-refracting medium, the ray curvature index, $\beta = -n'r/n$, is greater than unity. For a super-refracting spherical layer, the radius of curvature of the ray is less than the radius of curvature of the refracting surface. Super-refractivity occurs when $d\rho/dr = nk(1 - \beta) \leq 0$. The region where $d\rho/dr < 0$ should be evident from the data, and the critical value of dn/dr at the boundary is known, $dn/dr = -n/r \approx -157 \times 10^{-6} \text{ km}^{-1}$. Figure 6-11 shows a profile for a hypothetical refractivity gradient in the vicinity of a super-refracting layer. It could correspond to a narrow marine layer in the lower troposphere. Over the range $r_d \leq r \leq r_u$, the profile is super-refracting.

Figure 6-12 is a schematic showing the ray geometry for a super-refracting spherical layer with an upper boundary at $r = r_u$ and a lower boundary at $r = r_d$. Such layers are called ducts in ground-based radio transmission, and the word “ducting” is often used instead of “super-refracting.” Two critical rays are shown in this figure. The upper critical ray just grazes the top of the super-

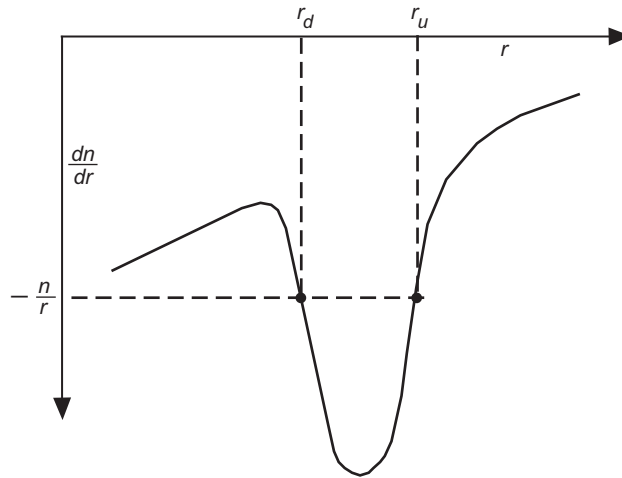


Fig. 6-11. Gradient of $n(r)$ near a super-refracting medium.

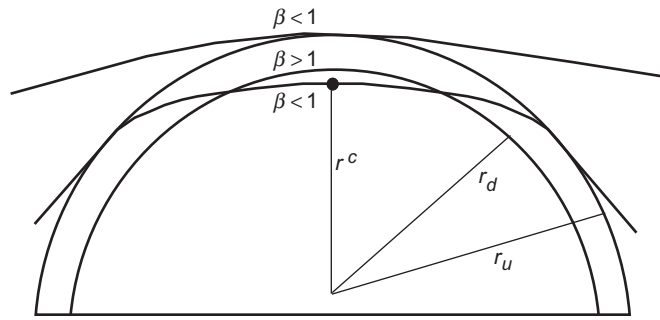


Fig. 6-12. Ray Geometry for a super-refracting spherical layer.

refracting layer; it has an impact parameter value of $n(r_u)r_u$. The lower critical ray has a tangency point at $r_* = r^c$ and an impact parameter value of $n(r^c)r^c$; it manages to escape from the top of the layer just before its ray path would have been turned inward by the strong refractive gradient in the layer. This lower critical ray escapes tangentially to the surface at $r = r_u$. It follows from Bouguer's law that the impact parameter for this critical ray is $n(r^c)r^c = n(r_u)r_u$. Thus, in geometric optics we have a discontinuity in the bending-angle profile versus impact parameter at this critical impact parameter value, $\rho_* = kn(r_u)r_u$. Two rays, one just grazing the top of the layer with $r_* = r_u$

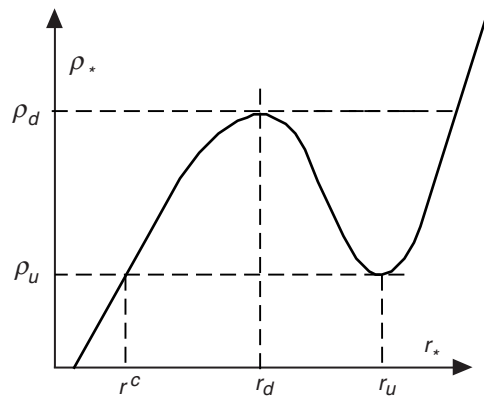


Fig. 6-13. Impact parameter curve in a super-refracting zone.

and the other at the lower critical tangency point $r_* = r^c$, both have the same impact parameter value but different bending angles. A ray with its turning point radius in the range $r^c < r_* < r_u$ cannot escape; for a ray to exist, the turning point radius r_* must either equal or exceed $r = r_u$, or it must be equal to or less than r^c .

Figure 6-13 shows an impact parameter curve $\rho_* = kn(r_*)r_*$ versus turning point radius r_* in the vicinity of a super-refracting layer. Note that $\rho_u < \rho_d$. A hypothetical ray with its tangency point in the range $r^c < r_* < r_u$ would have an impact parameter value in the range $\rho_u < \rho_* < \rho_d$. But from Fig. 6-13 we see that, in traveling along such a ray in the range $r_* \leq r \leq r_u$, one would eventually come to a point on the ray in the super-refracting layer past which $\rho(r) < \rho_*$, which is not allowed in geometric optics for a spherical geometry. See Appendix A, Eq. (A-4b). A necessary condition for the existence of a real ray between specified endpoints is that $\rho \geq \rho_*$ at *all* points along the ray. It is no good for $\rho \geq \rho_*$ to hold part of the way; it must hold all the way between end points, or else the term $(\rho^2 - \rho_*^2)^{1/2}$ in the bending angle and phase delay equations becomes imaginary at some point.

Figure 6-13 shows that the value of r^c relative to r_d depends on the difference $\rho_d - \rho_u$ and on the average slope of $d\rho/dr$ below the super-refracting layer. A first approximation is given by

$$r^c \approx r_d - (r_u - r_d) \frac{\bar{\beta}_{SR} - 1}{1 - \bar{\beta}^c} \quad (6.4-18)$$

where $\bar{\beta}^c < 1$ is the average value of β below the lower boundary of the super-refracting layer in the vicinity of $r = r^c$, and $\bar{\beta}_{SR} > 1$ is the average value of β in the super-refracting layer. If $\bar{\beta}^c$ is near unity, that is, nearly super-refracting, then the difference $r_d - r^c$ can be much larger than the thickness of the super-refracting layer itself.

For geometric optics, then, the refractivity profile in the range $r^c < r < r_u$ is terra incognita. Moreover, geometric optics already begins to fail⁶ before reaching these critical tangency point limits at $r_* = r^c$ and $r_* = r_u$.

No such restriction applies in wave theory, but a super-refracting layer does complicate matters. The point where $d\rho/dr = 0$ marks the boundary of a super-refractive layer, which necessitates breaking the integral in Eq. (6.4-6) for $2dG^\dagger(\nu)/d\nu$ into three sections, one section above the upper boundary at $\rho_u = kn(r_u)r_u$, one below the lower boundary at $\rho_d = kn(r_d)r_d$, and one through the layer where $d\rho/dr < 0$.⁷ Alternatively, one can write the integral in a less convenient form in terms of the radial coordinate itself. The end point of the integral becomes a function of $\rho^\dagger(\nu)/kn(r^\dagger)$. This has three roots for r^\dagger when ν lies within the range $\rho_u < \nu < \rho_d$: one above, $r > r_u$; one below, $r < r_d$; and one within the super-refractive layer, $r_d < r < r_u$.

Let us define the index of refraction profile according to regime:

$$n(r) = \begin{cases} n_1(r), & r \leq r_d \\ n_2(r), & r_d \leq r \leq r_u \\ n_3(r), & r_u \leq r \end{cases} \quad (6.4-19)$$

⁶ For a geometric optics version of a super-refractive boundary caused by a 5 percent discontinuity in refractivity, see Figs. 2-2(b) and 2-7(a). The predicted amplitude is exactly zero in the shadow zone. Figure 2-11 shows the scalar diffraction version. Figures 3-24 and 3-25 show the Mie scattering version.

⁷ Recall in Section 5.7, Eq. (5.7-27), that for a fixed spectral number ν we have set $\partial G[\rho, \nu]/\partial \rho = 0$ for $\rho \leq \rho^\dagger = \nu - \hat{y}^\dagger K_\rho$. This is an approximation that exploits the near-equality of $2dG[\rho^\dagger(\nu), \nu]/d\nu$ and $\alpha_L(\nu)$ in a medium with a moderate refractive gradient (see Appendix J). The error is small, but it depends on the curvature of the actual refractivity profile in the immediate vicinity of this turning point where the phase of the incoming wave is rapidly becoming stationary for decreasing $\rho < \nu$. See Fig. 5-7 for the exact phase profile $\partial \vartheta_i^-/\partial \rho$ in an Airy layer compared to $\partial G[\rho, \nu]/\partial \rho$. In a super-refractivity zone where $\rho_u < \nu < \rho_d$, we need the integral for $2dG^\dagger(\nu)/d\nu = 2dG[\rho^\dagger(\nu), \nu]/d\nu$ only for those sections where $\rho \geq \rho^\dagger(\nu)$. Hence the three sections.

Figure 6-14 is a sketch for $n(\rho)$ in the super-refracting zone. We have the continuity constraints $n_1(r_d) = n_2(r_d)$, $n_2(r_u) = n_3(r_u)$. If we now apply the wave theory version of the Abel transform in Eq. (6.4-15) to the Fourier observation function $F[\omega_v]$, we obtain

$$\begin{aligned} \frac{1}{\pi} \int_{v^\dagger(\rho_*)}^{\infty} \frac{\dot{\tilde{\theta}}_L F[\omega_v]}{\sqrt{v^2 - \rho_*^2}} dv &= \int_{\rho_*}^{\infty} \log n(\rho) W(\rho, \rho_*) d\rho = \\ &= \int_{\rho_*}^{\infty} \log n_3 W d\rho, \quad \rho_* \geq \rho_d, \\ &= \int_{\rho_*}^{\rho_d} (\log n_1 - \log n_2 + \log n_3) W d\rho + \int_{\rho_d}^{\infty} \log n_3 W d\rho, \quad \rho_u \leq \rho_* \leq \rho_d, \\ &= \int_{\rho_*}^{\rho_u} \log n_1 W d\rho + \int_{\rho_u}^{\rho_d} (\log n_1 - \log n_2 + \log n_3) W d\rho + \int_{\rho_d}^{\infty} \log n_3 W d\rho, \quad \rho_* \leq \rho_u \end{aligned} \quad (6.4-20)$$

If we replace $W(\rho, \rho_*)$ by the Dirac delta function, Eq. (6.4-20) becomes

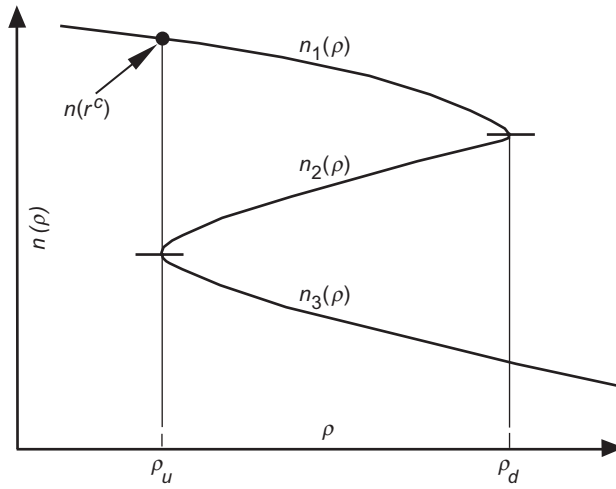


Fig. 6-14. Profile for n versus ρ in a super-refracting zone.

$$\frac{1}{\pi} \int_{v^\dagger(\rho_*)}^{\infty} \frac{\dot{\theta}_L F[\omega_v]}{\sqrt{v^2 - \rho_*^2}} dv \doteq \begin{cases} \log n_3(\rho_*), & \rho_* \geq \rho_d, \\ \log n_1(\rho_*) - \log n_2(\rho_*) + \log n_3(\rho_*), & \rho_u \leq \rho_* \leq \rho_d, \\ \log n_1(\rho_*), & \rho_* \leq \rho_u \end{cases} \quad (6.4-21)$$

For spectral numbers lying in the region $\rho_u \leq v \leq \rho_d$, only the combination $N_1(\rho_*) - N_2(\rho_*) + N_3(\rho_*)$ is recoverable with this approach.

6.4.2 Improving the Accuracy of $G^\dagger(v)$

One can refine the approximation in Eq. (5.7-27) for $G^\dagger(v)$ by forcing $G[\rho, v]$ to align with the exact form for the phase delay in an Airy layer. Per the discussion concerning Eqs. (5.7-24) and (5.7-25), $\vartheta_l^-(\rho)$ gives the phase delay of the l th spectral coefficient $a_l^-(\rho)$ for an incoming wave in an Airy layer. One aligns $G[\rho, v]$ with $\vartheta_l^-(\rho)$ at a radial distance ρ where $G[\rho, v]$ is still accurate. The form for $\vartheta_l^-(\rho)$ is given by

$$\vartheta_l^-(\rho) = \tan^{-1} \left(\mp \frac{\text{Bi}[\tilde{y}]}{\text{Ai}[\tilde{y}]} \right) - \tan^{-1} \left(\frac{\text{Bi}[\hat{y}]}{\text{Ai}[\hat{y}]} \right) + \text{constant} \quad (6.4-22)$$

where \tilde{y} is defined in Eq. (5.7-18) for an Airy layer, and $\tilde{y}/\hat{y} = 1 - \beta l^{-2/3}$. The top sign in Eq. (6.4-22) applies to a super-refracting medium where $\beta > 1$; the bottom sign applies when $\beta < 1$. One can readily show that the asymptotic forms for $\vartheta_l^-(\rho)$ and $G[\rho, v]$ for negative values of \hat{y} are identical in an Airy layer. See Fig. 5-7. For decreasing $\rho < v$, note that $\vartheta_l^-(\rho) - \vartheta_l^-(0)$ rapidly approaches zero.

From Eq. (6.4-22), we have

$$\frac{\partial \vartheta_l^-(\rho)}{\partial v} \doteq \frac{1}{\pi K_v} \left(\frac{\mp \tilde{y}}{\text{Ai}[\tilde{y}]^2 + \text{Bi}[\tilde{y}]^2} - \frac{\hat{y}}{\text{Ai}[\hat{y}]^2 + \text{Bi}[\hat{y}]^2} \right) \frac{1}{\hat{y}} + \text{constant} \quad (6.4-23)$$

To align $\partial G[\rho, v] / \partial v$ with $\partial \vartheta_l^- / \partial v$ in the vicinity of $\rho = v$, one sets $\partial G[\rho, v] / \partial v$ according to the following schedule:

$$\frac{\partial G[\rho, \nu]}{\partial \nu} \Rightarrow \left\{ \begin{array}{l} \frac{\partial G[\rho, \nu]}{\partial \nu}, \quad \rho \geq \rho^\diamond = \nu + \hat{y}^\diamond K_\nu \\ \frac{\partial G[\rho^\diamond, \nu]}{\partial \nu} + \left(\frac{\partial \vartheta_l^-(\rho)}{\partial \nu} - \frac{\partial \vartheta_l^-(\rho^\diamond)}{\partial \nu} \right), \quad \rho \leq \rho^\diamond \end{array} \right\} \quad (6.4-24)$$

The chosen value of \hat{y}^\diamond is a compromise, taking into account on one hand the impending failure of $g(\hat{y})$ to provide the correct phase delay for $a_l^-(\rho)$ for increasing \hat{y} near zero, and on the other hand the decreasing accuracy of the Airy layer approximation to the actual refractivity profile if applied over too wide an altitude range. Equation (6.4-23) shows that $\partial(\vartheta_l^-(\rho) - \vartheta_l^-(0))/\partial \nu$ also rapidly approaches zero for decreasing $\rho < \nu$. Thus, we are concerned about the Airy layer approximation over a relatively narrow altitude range. The Airy layer approximation should be valid over the altitude range $\sim -2K_\nu \leq \rho - \nu \leq -\hat{y}^\diamond K_\nu$, about 50 m. Here we have set $\hat{y}^\diamond = -2$. With this modified form, the derivative of the spectral density function becomes

$$\begin{aligned} \frac{dG^\dagger}{d\nu} &\Rightarrow \frac{\partial G[0, \nu]}{\partial \nu} \Rightarrow \frac{\partial G[\rho^\diamond, \nu]}{\partial \nu} + \left(\frac{\partial \vartheta_l^-(0)}{\partial \nu} - \frac{\partial \vartheta_l^-(\rho^\diamond)}{\partial \nu} \right) = \\ &\frac{\partial G[\rho^\diamond, \nu]}{\partial \nu} - \frac{1}{\pi K_\nu} \left(\frac{\mp \tilde{y}^\diamond}{\text{Ai}[\tilde{y}^\diamond]^2 + \text{Bi}[\tilde{y}^\diamond]^2} - \frac{\hat{y}^\diamond}{\text{Ai}[\hat{y}^\diamond]^2 + \text{Bi}[\hat{y}^\diamond]^2} \right) \frac{1}{\hat{y}^\diamond} \end{aligned} \quad (6.4-25)$$

The weighting function $W(\rho, \rho_*)$ also is slightly modified. In this regard, note that the corrective term from the Airy layer in Eq. (6.4-25) approaches zero as β approaches zero with increasing impact parameter.

The difference in the two forms for $dG^\dagger/d\nu$ in Eqs. (6.4-2) and (6.4-25) is given by

$$\begin{aligned} \Delta \left(\frac{dG^\dagger}{d\nu} \right) &= -\pi K_\nu \int_{\rho^\dagger}^{\rho^\diamond} \frac{d \log n}{d\rho} (\text{Ai}[\hat{y}]^2 + \text{Bi}[\hat{y}]^2) d\rho + \frac{\partial \vartheta_l^-(\rho^\diamond)}{\partial \nu} - \frac{\partial \vartheta_l^-(0)}{\partial \nu} \\ &\doteq \frac{d \log n}{d\rho} g(\hat{y}^\diamond) + \frac{1}{\pi \hat{y}^\diamond K_\nu} \left(\frac{\mp \tilde{y}^\diamond}{\text{Ai}[\tilde{y}^\diamond]^2 + \text{Bi}[\tilde{y}^\diamond]^2} - \frac{\hat{y}^\diamond}{\text{Ai}[\hat{y}^\diamond]^2 + \text{Bi}[\hat{y}^\diamond]^2} \right) \\ &\rightarrow \frac{1}{K_\nu} \left(\frac{\beta}{\beta-1} \right) \left(\frac{6-5\beta}{32} \right) (-\hat{y}^\diamond)^{-5/2} + O[(-\hat{y}^\diamond)^{-4}] \end{aligned} \quad (6.4-26)$$

To the extent that the Airy layer approximation is valid, this form gives the error in Eq. (6.4-2) for $dG^\dagger/d\nu$. For $\beta = 0.5$, this difference is about 0.1 mrad

at $\hat{y}^\diamond = -2$; for $\beta = 2$, it is about 0.2 mrad. The error increases as $\beta \rightarrow 1$. The Airy layer analysis in Section 5.7 fails at $\beta = 1$, exactly.

With this modification, one still ends up with an integration interval over ρ that is effectively truncated from below at $\rho = \nu - \hat{y}^\diamond K_\nu$ instead of at $\rho = \nu - \hat{y}^\dagger K_\nu$. A super-refractivity zone still yields three separate integration sections for $dG^\dagger(\nu)/d\nu$ when the spectral number lies in the super-refractivity zone $kn(r_u)r_u < \nu < kn(r_d)r_d$: one section above $r = r_u$, one below $r = r_u$ down to $r = r_d$, and one below $r = r_d$ down to the turning point. See also the discussion in Section 5.8 on comparison of the wave equation solutions in a super-refracting medium.

6.4.3 Resolution Issues

One could infer from Eq. (6.4-15) that away from a super-refracting region the resolution with which $n(\rho)$ may be recovered is limited only by the SNR measurement errors present in the Fourier transform quantity $F[\omega]$. But there are a number of implicit assumptions embedded in Eq. (6.4-15), not the least of which are the assumptions of spherical symmetry and error-free ionosphere effects. These and other resolution-limiting factors have been discussed in [8,9]. Departures from spherical symmetry arise in two forms: a first part, largely deterministic, is due to departures of the geopotential of the Earth from spherical symmetry, the oblateness being the principal term. The latitude-dependent Earth-flattening term is factored into the spectral formulation presented here by a small adjustment to the value of r_o and to the satellite coordinates. The second part is due to imperfect a priori knowledge of the topography of any given surface of constant refractivity—along-track water vapor variability, for example. Another contributor is the geostrophic effect from winds aloft on a surface of constant pressure. Ad hoc calibrations could be used to correct for these usually small effects for each occultation, using some local model from European Centre for Medium-Range Weather Forecasts (ECMWF), for example—not an impossible task, but surely a tedious one. In a thin phase screen model, these adjustments are equivalent to adjusting D , the limb distance, by an amount δD . It can be shown [8,9] that an uncertainty or error δD in the adopted value of D degrades the resolution Δh in the screen and that $\delta(\Delta h)/\mathcal{F}_o$ is at least as large as $0.45(\delta D/D)^{1/2}$, where \mathcal{F}_o is the vertical diameter of the free space first Fresnel zone, about 1.5 km. Thus, a 1 percent error in D maps into a limiting vertical resolution that is about 5 percent of \mathcal{F}_o ; a 4 percent error maps into about 10 percent, and so on. With respect to the local Fresnel limit, these percentages would be greater by the factor $\zeta^{-1/2}$ because of defocusing. In other words, the limiting resolution is quite sensitive to this type of error.

Similar conclusions follow for other resolution-limiting factors. The horizontal resolution is limited by the vertical resolution [see Eq. (2.2-10)]. But the vertical resolution is limited in effect by the horizontal resolution, as just discussed. Equating these two expressions containing δD yields

$$\delta D \approx 90 \left(\frac{\zeta}{(1-\beta)^2} \right)^{1/3} \text{ km} \quad (6.4-27)$$

This gives a minimum horizontal resolution of about 50 km where the defocusing is 1/10 and $\beta = 0.2$, and of about 100 km where the defocusing is 1. This limiting horizontal resolution yields a limiting vertical resolution that is 15 to 20 percent of the local Fresnel diameter. That the Fresnel limit on vertical resolution can be substantially surpassed using scalar diffraction theory techniques (30 to 100 m) has already been demonstrated [8,10–12], but a realistic limit is yet to be established.

Another consideration is the cross-track and along-track drifts of the tangency point during its descent or ascent. The velocity vector of the tangency point of an occultation is rarely exactly vertical in the upper atmosphere; it is canted off-vertical depending on the orbit geometry of the satellites. The cross-track velocity of the tangency point is proportional to the tangent of this off-vertical angle. Moreover, the vertical component of the tangency point velocity vector slows because of defocusing. But, the cross-track component of the drift is not appreciably slowed, and the along-track component accelerates with depth, approaching the rate $-\rho_* d\tilde{\theta}_L / dt$ in strong defocusing. These factors result in a progressively more shallow descent ratio with depth for the tangency point. In other words, the horizontal displacement of the tangency point during an occultation is a significant factor in resolution questions. Of course, in a 4DVAR context, these resolution issues should be addressed in terms of the information content already extant in the 4DVAR system.

6.5 Summary

This section outlines one spectral technique based on wave theory for recovering the refractivity profile $N(\rho)$ from the spectral derivative of the Fourier transform of the received amplitude and stopped phase measurements made by the LEO over time. Coincidentally, the bending-angle profile $\alpha_L(\nu)$ is recovered. Spectral techniques in general facilitate recovery of bending angles and refractivity fundamentally because of their ability to uniquely sort received rays according to their excess Doppler or to their impact parameter values in a spherical symmetric medium. Spectral techniques seem essential when adverse signal conditions prevail because of the concurrent reception of multiple rays. Spectral techniques also are efficacious, but perhaps not essential if a third-

order ray theory is used in near-caustic situations where the validity of second-order geometric optics breaks down.

Because of the close correspondence noted in Table 5-1 between the phase delay spectral density function $2G^\dagger(\nu)$ evaluated at its stationary value in spectral number and the scalar diffraction/thin-screen phase function $\varphi(\rho_*)$ discussed in Chapter 2, one need not start from wave theory as the framework for obtaining these spectral results. We noted in Section 5.10 that the phase delay spectral density function $G^\dagger(\nu)$ from wave theory and the thin-screen phase function $\varphi(h)$ are related by

$$-2G^\dagger(\nu) \doteq 2 \int_{\nu}^{\infty} \tilde{\alpha}(\nu, \nu) d\nu = \int_{\nu}^{\infty} \alpha_L(\nu) d\nu \Leftrightarrow \varphi(\nu) \quad (6.5-1)$$

The analog of Ψ_{Lo} in the thin screen is $\Phi(h, h_{LG})$, the Fresnel phase function given in Eq. (2.5-1). It follows that essentially the same form given in Eq. (6.4-5) would come from the scalar diffraction integral in a thin phase screen model, provided the screen is so constructed that there is a one-to-one relationship between h and the impact parameter. Therefore, with this caveat in mind, the wave-theoretic Fourier approach followed here in Chapter 6 to recover the refractivity profile could be converted into a thin-screen Fourier approach by replacing $-2G^\dagger(\nu)$ with $\varphi(\rho_*)$ and its derivative $2dG^\dagger(\nu)/d\nu$ with $-d\varphi(\rho_*)/d\rho_*$, that is, with $\alpha_L(\rho_*)$. One also can start from a thin phase screen model, whose surface is defined by the impact parameter, and use scalar diffraction theory to obtain essentially the same results. This offers an easier approach when the thin-screen model is caustic-free.

Finally, an intriguing prospect for future in-receiver signal processing operations in support of limb sounding is the incorporation of advanced processing techniques, such as essentially real-time Fourier transform algorithms. With current POD information, a smart receiver not only could power through adverse signal episodes and perform backward (in time) reconstruction, it also could report bending angles for multiple rays and refractivity profiles directly, along with essential statistics, basic phase and amplitude data, and other housekeeping information.

One should not underestimate the potential cost savings of an in-receiver automated system using the GPS, especially in adverse signal conditions. For an analogy, one need look no further than the navigation of a typical LEO with an onboard GPS receiver. Here one can find highly automated processes resulting in centimeter-level orbit accuracy [13]. Once operational, the workforce required to routinely maintain and use this capability is an order of magnitude smaller than that required for most ground-based tracking systems [14]. Investment now in the necessary research and development to enable future automated in-receiver operations for GPS-based limb sounding would

seem to be a wise programmatic option. In the future, other global navigation satellite system programs besides the GPS will become operational. Use of these systems also should be incorporated in future flight receiver designs.

References

- [1] R. Anthes, C. Rocken, and Y. H. Kuo, "Applications of COSMIC to Meteorology and Climate," *Terrestrial, Atmospheric and Ocean Sciences*, vol. 11, pp. 115–156, 2000.
- [2] T. Yunck, C. H. Liu, and R. Ware: "A History of GPS Sounding," *Terrestrial, Atmospheric and Ocean Sciences*, vol. 11, pp. 1–20, 2000.
- [3] J. Thomas, *Signal-Processing Theory for the TurboRogue Receiver*, JPL Publication 95-6, Jet Propulsion Laboratory, Pasadena, California, 1995.
- [4] C. Ao, T. Meehan, G. Hajj, A. Mannucci, and G. Beyerle, "Lower Troposphere Refractivity Bias in GPS Occultation Retrievals," submitted to *Journal of Geophysical Research*, 2003.
- [5] J. Jackson, *Classical Electrodynamics*, 2nd ed., New York, New York: J. Wiley & Sons, Inc., 1975.
- [6] G. Lindal, J. Lyons, D. Sweetnam, V. Eshelman, D. Hinson, and G. Tyler, "The Atmosphere of Uranus: Results of Radio Occultation Measurements with Voyager 2," *Journal of Geophysical Research*, vol. 92, pp. 14,987–15,001, 1987.
- [7] S. Sokolovskiy, "Modeling and Inverting Radio Occultation Signals in the Moist Troposphere," *Radio Science*, vol. 36, no. 3, pp. 441–458, 2001.
- [8] E. Marouf, G. Tyler, and P. Rosen, "Profiling Saturn's Rings by Radio Occultation," *Icarus*, vol. 68, pp. 120–166, 1986.
- [9] W. Melbourne, E. Davis, C. Duncan, G. Hajj, K. Hardy, E. Kursinski, T. Meehan, L. Young, and T. Yunck, *The Application of Spaceborne GPS to Atmospheric Limb Sounding and Global Change Monitoring*, JPL Publication 94-18, Jet Propulsion Laboratory, Pasadena, California, 1994.
- [10] E. Karayel and D. Hinson, "Sub-Fresnel Scale Vertical Resolution in Atmospheric Profiles from Radio Occultation," *Radio Science*, vol. 32, no. 2, pp. 411–423, 1997.
- [11] M. Gorbunov, A. Gurvich, and L. Bengtsson, *Advance Algorithms of Inversion of GPS/MET Satellite Data and Their Application to Reconstruction of Temperature and Humidity*, Max Planck Institute for Meteorology, Report 211, Hamburg, Germany, 1996.

- [12] K. Igarashi, K. Pavelyev, J. Wickert, K. Hocke, and D. Pavelyev, "Application of Radio Holographic Method for Observation of Altitude Variations of the Electron Density in the Mesosphere/Lower Thermosphere Using GPS/MET Radio Occultation Data," *Journal of Atmospheric and Solar-Terrestrial Physics*, vol. 64, pp. 959–969, 2002.
- [13] R. Muellerschoen, A. Reichert, D. Kuang, M. Heflin, W. Bertinger, and Y. Bar-Sever, "Orbit Determination with NASA's High Accuracy Real-Time Global Differential GPS System," ION GPS2001, September 11–14, 2001, Salt Lake City, Utah.
- [14] W. Melbourne, T. Yunck, W. Bertiger, B. Haines, and E. Davis, "Scientific Applications of GPS on Low Earth Orbiters," *Zeitschrift für Satellitengestützte Positionierung, Navigation und Kommunikation*, vol. 4, pp. 131–145, 1993.